

3D CMZ V: A new orbital model of our Galaxy’s Center, informed by data across the electromagnetic spectrum

DANI R. LIPMAN,¹ CARA BATTERSBY,^{1,2} DANIEL WALKER,^{3,1} MAÏCA CLAVEL,⁴ B.L. DUBOIS,² ADAM GINSBURG,⁵
JONATHAN D. HENSHAW,⁶ RALF S. KLESSEN,^{7,8} ELISABETH A.C. MILLS,⁹ FRANCISCO NOGUERAS-LARA,¹⁰
MATTIA C. SORMANI,¹¹ AND ROBIN G. TRESS¹²

¹*University of Connecticut, Department of Physics, 196A Hillside Road, Unit 3046 Storrs, CT 06269-3046, USA*

²*Center for Astrophysics | Harvard & Smithsonian, MS-78, 60 Garden St., Cambridge, MA 02138 USA*

³*UK ALMA Regional Centre Node, Jodrell Bank Centre for Astrophysics, Oxford Road, The University of Manchester, Manchester M13 9PL, United Kingdom*

⁴*Univ. Grenoble Alpes, CNRS, IPAG, 38000 Grenoble, France*

⁵*Department of Astronomy, University of Florida, P.O. Box 112055, Gainesville, FL 32611, USA*

⁶*Max-Planck-Institut für Astronomie, Königstuhl 17, D-69117, Heidelberg, Germany*

⁷*Universität Heidelberg, Zentrum für Astronomie, Institut für Theoretische Astrophysik, Albert-Ueberle-Str. 2, 69120 Heidelberg, Germany*

⁸*Universität Heidelberg, Interdisziplinäres Zentrum für Wissenschaftliches Rechnen, Im Neuenheimer Feld 225, 69120 Heidelberg, Germany*

⁹*Department of Physics and Astronomy, University of Kansas, 1251 Wescoe Hall Drive, Lawrence, KS 66045, USA*

¹⁰*Instituto de Astrofísica de Andalucía (CSIC), Glorieta de la Astronomía s/n, 18008 Granada, Spain*

¹¹*Como Lake centre for AstroPhysics (CLAP), DiSAT, Università dell’Insubria, via Valleggio 11, 22100 Como, Italy*

¹²*Institute of Physics, Laboratory for Galaxy Evolution and Spectral Modelling, EPFL, Observatoire de Sauverny, Chemin Pegasi 51, 1290 Versoix, Switzerland*

ABSTRACT

The 3D structure of The Milky Way’s Central Molecular Zone (CMZ) informs our understanding of star formation cycles, black hole accretion, and the evolution of galactic nuclei. However, a comprehensive 3D model has remained elusive, as no singular dataset nor theory contains the requisite information to describe the orbital motion of the gas. We implement a Bayesian framework to flexibly combine datasets across the electromagnetic spectrum for molecular clouds in our CMZ catalog. We develop near/far metrics for each dataset, including dust extinction, absorption, stellar densities, X-ray echoes, and proper motions; and report a posterior positional probability density function (PPDF) for each cloud. We then use the posterior PPDF distributions for all CMZ clouds to search for a best fitting x_2 orbit. We find that no single orbit is a perfect fit, but the structure can overall be represented by nested x_2 orbits, with major axes ranging from about $72 < a < 146$ pc. We also present projected line of sight distance estimates for all 31 clouds in the catalog. Our results highlight asymmetries along the line of sight, with most clouds lying on the near side of the Galactic Center, and agree overall with current near/far assumptions for most CMZ clouds, including those in the Sgr A region, which may be much closer to the center. We conclude that the CMZ can be well-described by x_2 orbital families, and that the overall gas distribution is more complex than a single closed or open elliptical orbit.

Keywords: CMZ — Galactic Center

1. INTRODUCTION

The inner 300 pc of the Milky Way, (the Central Molecular Zone, CMZ) is the central depot of the Galaxy, where gas from the disk is funneled inward via Galactic bar lanes, connecting to elliptical x_2 orbits aligned perpendicular to the bar. The CMZ exhibits extreme physical properties compared to the Galactic disk, including typical volume densities $> 10^4 \text{ cm}^{-3}$, as well as

temperatures, degrees of turbulence, and magnetic fields that tend to be 1-2 orders of magnitude higher compared to the solar neighborhood (e.g. Pillai et al. 2015; Krieger et al. 2017; Ginsburg et al. 2016; Mills et al. 2018; Butterfield et al. 2024, see Henshaw et al. (2023) for extensive review). The CMZ’s extreme properties also share some similarities with high redshift galaxies (Kruijssen & Longmore 2013; Henshaw et al. 2023), making it an ideal local laboratory for testing whether star forma-

tion varies as a function of environment. As our closest galaxy center at a distance of ~ 8.2 kpc (GRAVITY Collaboration et al. 2021), the Milky Way’s CMZ offers an opportunity to study the complicated interplay between gas inflows, star formation, and outflows in the centers of galaxies.

Most of the dense gas in the CMZ is thought to lie on an orbit of ~ 100 pc (i.e. the 100 pc stream or 100 pc ring) (e.g. Binney et al. 1991; Molinari et al. 2011; Kruijssen et al. 2015; Sormani et al. 2015). Simulations suggest that trace amounts of gas continue to fall inward onto the circumnuclear disk (CND), a ring of gas filling an inner $1\text{pc} < R_{\text{gal}} < 10\text{pc}$ annulus of the Galactic Center (GC), at a rate of $\sim 0.01 - 0.1 M_{\odot}\text{yr}^{-1}$ (Tress et al. 2020, 2024). The low amount of inflow towards the inner few parsecs near the supermassive black hole, SgrA*, is supported by the relatively low extinction in this region (Nogueras-Lara 2022). However, the mechanisms for transporting gas from the 100 pc ring to the CND are still debated (e.g. Shlosman et al. 1989; Balbus & Hawley 1998; Davies et al. 2007; Kim & Elmegreen 2017; Tress et al. 2020, 2024). The 3D geometry and orbital motions of CMZ gas is integral to modeling nuclear inflow, and thus impacts our understanding of star formation cycles (whether suppressed or periodic), black hole feeding, and the evolution of galactic nuclei.

The top-down shape of the CMZ has been described by four main theories: (i) two inner spiral arms (Sofue 1995, 2022; Sofue et al. 2025), (ii) a closed ellipse assuming a constant orbital velocity (Molinari et al. 2011), (iii) an open stream of orbits (Kruijssen et al. 2015), or (iv) a closed x_2 ellipse assuming constant angular momentum (Binney et al. 1991; Sormani et al. 2015; Tress et al. 2020; Chaves-Velasquez et al. 2025). Distinguishing between orbital models requires information to differentiate objects on either the near side (in front of SgrA*) or far side (behind), which can be used to determine the accuracy of each model (e.g. Henshaw et al. 2016b; Walker et al. 2025; Lipman et al. 2025).

Several studies have sought to determine approximate near/far locations of CMZ structures. For example, Sgr B2 has been strongly constrained to reside in the foreground via parallax measurements (Reid et al. 2009) and relative strengths of CO emission and OH absorption features (Yan et al. 2017). The Brick cloud also lies on the near side based on color-magnitude diagrams (Nogueras-Lara et al. 2021) and proper motion measurements (Martínez-Arranz et al. 2022). Most of these previous studies confirm that clouds reside within the CMZ, but are unable to quantify their relative positions. On the other hand, time delays of reflected X-ray radiation due to past flaring events from SgrA* have further con-

strained near-side positions of Sgr B2, as well as clouds in the Sgr A region (e.g. Ponti et al. 2010; Clavel et al. 2013; Chuard et al. 2018). More recent studies of stellar kinematics have also produced promising distance estimates for the 20 and 50 km s^{-1} clouds (Nogueras-Lara et al. 2026). However, these methods only provide distance estimates for a handful of clouds and, in the case of X-ray echoes, involve large systematic uncertainties. Lastly, Henshaw et al. (2016b) describes the overall distribution of dense molecular gas in the CMZ in position-position-velocity (PPV) space, but line of sight distances and relative positions of prominent structures have not been obtainable through these methods alone.

In a previous paper of this series, Lipman et al. (2025), we combined dust extinction techniques and molecular line absorption analysis from Walker et al. (2025) to obtain the near/far positions of clouds in our CMZ catalog and compare to proposed orbital models. We found that an x_2 model (as described in point iv above) generally fit the dense gas in the CMZ in both position-position (PP) and position-velocity (PV) space. Simulations of Milky Way-like galaxies produce similar star-forming rings and suggest that, on average, the gas can be approximated by a simple x_2 ellipse (Armillotta et al. 2019; Salas et al. 2020; Sormani et al. 2020b; Tress et al. 2020, 2024). Nuclear rings are also seen in many nearby galaxy centers (e.g. Sun et al. 2020; Stuber et al. 2023; Sun et al. 2024) and modeling of external CMZs has shown reasonable fittings to x_2 orbits (Levy 2022).

This paper builds on the analysis of Battersby et al. (2025a,b); Walker et al. (2025) and Lipman et al. (2025) (hereafter *Paper I*, *Paper II*, *Paper III*, and *Paper IV*). In this paper, we present a Bayesian framework to synthesize available near vs. far (NF) position data for molecular clouds in the CMZ, and use the posterior NF distributions to find a best fitting x_2 orbital model, as summarized in the schematic in Figure 1. In Section 2 we describe the data used for this work, including brief descriptions of relevant results and data products from papers I-IV. In Section 3 we design a Bayesian framework to determine posterior NF likelihoods for the cataloged clouds (Figure 1 panels 1 and 2), and introduce a minimization method for fitting a 4D (ℓ , b , v , NF) x_2 orbital model of the CMZ (panel 3). We present our results in Section 4. In Section 5, we discuss the relative positions of CMZ clouds based on our best fits (panel 4). We also discuss the morphology of the CMZ based on our projected model and interpretations for various structures in PPV space. We address uncertainties and limitations of our methods in Section 6, and summarize our conclusions in Section 7.

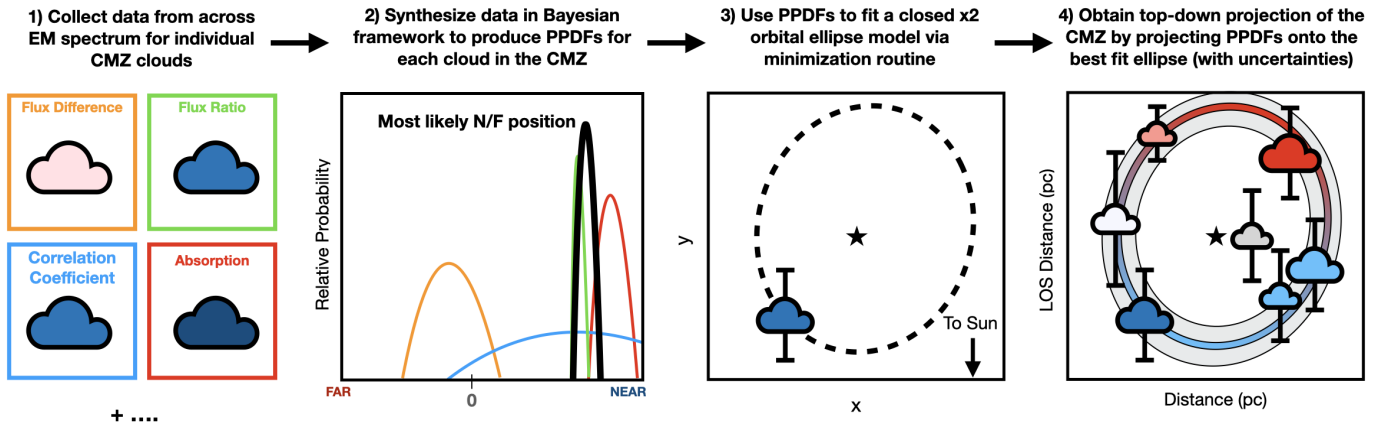


Figure 1. We present a method to synthesize multi wavelength datasets to obtain most likely near/far positions of clouds in the CMZ, and find a best-fitting elliptical orbit. Our methodology follows the above schematic from left to right: 1) we collect both near/far and line of sight distance constraints from a variety of methods across the electromagnetic spectrum (Section 2), 2) we build a Bayesian framework to combine these different data on a normalized near-to-far scale, producing positional probability density functions which peak at the most likely position of a given cloud (Section 3.1), 3) Find a best fitting closed elliptical x_2 orbit using each cloud’s PPV location and NF distribution (Section 3.2), 4) Use the best fit orbital model to present a preliminary top-down projection of the CMZ with line-of-sight distance estimates for all CMZ clouds (Section 4.3). The black star in panels 3 and 4 indicates the location of SgrA*. The blue and red colors of clouds in panels 3 and 4 indicate likely near or far positions, respectively.

2. USING DATASETS ACROSS THE ELECTROMAGNETIC SPECTRUM TO DERIVE NEAR/FAR LIKELIHOODS

We combine datasets from multiple wavelengths and synthesize them to generate posterior positional probability density functions for the locations of each molecular cloud in our CMZ catalog. NF positions of clouds were determined from molecular line and MIR datasets in *Paper III* and *Paper IV*. In addition to these methods, we incorporate NF positions from star counts, and distance constraints for a handful of clouds based on X-ray data and stellar kinematics. In the following sections, we describe the datasets and products used for deriving NF likelihoods. The datasets available for each cloud are listed in the second to last column of Table 1.

2.1. CMZ column density map and cloud catalog

The catalog used for the analysis in this work identifies the densest molecular clouds in the CMZ based on integrated column density maps created using observations from the Herschel Infrared Galactic Plane (Hi-GAL) Survey (Molinari et al. 2010, 2016). Details for the creation of the column density map can be found in the previous papers of this series. Described briefly: *Paper I* performed a modified blackbody fit to HiGAL data covering the inner 40° of the Milky Way, and produced integrated column density and temperature maps. *Paper II* produced a hierarchical catalog of structures in the column density map using the `astrodendro` Python package (Robitaille et al. 2019). We then calculated and tabulated properties and SFRs for the hierarchy of CMZ

structures, and placed the CMZ in a global context with respect to the Milky Way and other galaxies. *Paper III* builds upon the catalog by identifying a consistent sample of clouds in PPV space. Nine clouds in the catalog contained multiple velocity components in the HNC/O emission not seen in H_2CO . Those clouds were divided into separate spatial masks based on the projected peak intensity of the velocity components. Lastly, *Paper III* presents a detailed kinematic study of each cloud and produced masks corresponding to each dendrogram leaf, which we use in this paper. The column density map from *Paper I* and cloud masks and ID numbers from *Paper III* are shown in the top panel of Figure 2. The first five columns of Table 1 from *Paper III* (cloud IDs, cloud names, and central (ℓ, b, v) positions) are summarized in Table 1.

2.2. Near/far distinctions from absorption and extinction methods

The previous papers in this series distinguished between proposed CMZ models by determining the likely NF positions of all cataloged molecular clouds, and comparing them to different orbital geometries. The analyses leverage the strong absorption at mid-infrared wavelengths, as cold dust absorbs the bright emission from the CMZ, making the material in front appear as dark extinction features. The difference in the bright Galactic background and observed emission are large enough to estimate NF positions of clouds in the CMZ based on molecular line absorption (*Paper III*) or dust extinction (*Paper IV*). We briefly summarize the general concepts

of the methods here, and refer the reader to the previous papers in the series for more detailed explanations.

Paper III quantifies the NF positions of CMZ clouds by assuming a uniform background of diffuse free-free and synchrotron emission in the CMZ. This assumption implies that clouds in front of the continuum will show strong molecular absorption features, while clouds behind show little to no absorption. NF positions of clouds are obtained by comparing molecular line absorption against the radio continuum measured toward each cloud. For this study, we utilize the masked fractional absorption values reported in Table 2 of *Paper III* as a NF indicator from absorption.

Paper IV introduces three dust extinction techniques to determine NF positions of CMZ clouds by using dark MIR features, seen in Spitzer $8\mu\text{m}$ (Benjamin et al. 2003; Churchwell et al. 2009) and HiGAL $70\mu\text{m}$ images (Molinari et al. 2010). The $8\mu\text{m}$ dust extinction analysis assumes a constant foreground and background, offset by inhomogeneous emission from the bright CMZ. Clouds in the CMZ absorb and re-emit this background at different wavelengths. Thus, clouds on the near side appear as dark extinction features, while clouds on the far side may appear similar to or brighter than the background. The analysis of *Paper IV* presents: 1) a flux difference between $8\mu\text{m}$ emission and a smoothed background, and 2) a flux ratio between the $8\mu\text{m}$ emission and smoothed map. Additionally, *Paper IV* uses optically thin $70\mu\text{m}$ data to determine the correlation between the cloud column density maps and the amount of material associated with extinction. In this paper, we use the flux difference, flux ratio, and Pearson correlation coefficient of emission and extinction column densities for each CMZ catalog cloud, as reported in Table 1 of *Paper IV*.

2.3. Near/far distances from star counts

We introduce another method for NF distinction of CMZ clouds based on stellar density maps from Nishiyama et al. (2013), which report the number of non-foreground stars with extinction-corrected $K_{s,0} > 10.5$. The authors combine data from the NIR camera SIRIUS (Nagayama et al. 2003) on the 1.4m telescope IRSF, and $2.25\mu\text{m}$ images from ISAAC at the ESO VLT (Nishiyama & Schödel 2013) to supplement the crowded inner $1'$. The SIRIUS data cover the central $840\text{ pc} \times 280\text{ pc}$ of the Galaxy, and have 10σ limiting magnitudes of $(H, K_s) \sim (16.6, 15.6)$ and extinction $A(K_s) \sim 2 - 3.5$

mag. Extinction-corrected stellar density maps were created for the central $20' \times 20'$ field, achieving completeness for $K_s > 10.5$ of $\sim 97\%$ (Hatano et al. 2013; Yasui et al. 2015). The data are divided into $2'$ bins to create a map of the number of stars per arcmin^2 .

The stellar density map of the CMZ from Nishiyama et al. (2013) (top panel of Figure 2) shows areas of lower star counts compared to the expected background, where dense molecular clouds in front of the GC block the stars behind. The stellar distribution in this region is dominated by the Galactic bulge and nuclear stellar disk (NSD), a flat disk of stars with a total mass of $\sim 1.05 \times 10^9 M_\odot$, which overlaps with the CMZ between a range of $30 < R_{\text{gal}} < 300\text{ pc}$ (Launhardt et al. 2002; Sormani et al. 2020a, 2022). We use a ratio of the observed star counts to a modeled stellar distribution from the Galactic bulge and NSD for a quantitative measure of how many stars are being extinguished by the dense molecular clouds. For a near-sided cloud, we expect the median ratio to be < 1 , as the cloud blocks the star light expected from the model, while far-sided clouds would have ratios > 1 . A ratio of 1 implies an exact match to the expected bulge and NSD distribution without a molecular cloud present.

To model the expected star counts, we use the stellar distribution model from Gallego-Cano et al. (2020). The authors present a best fit to the Nishiyama et al. (2013) data after masking out regions of low density. They also mask out the Nuclear Stellar Cluster (NSC), a massive ($M \simeq 2.5 \times 10^7 M_\odot$) and dense disk of stars in the central 10 pc (Genzel et al. 2010; Schödel et al. 2014). The model is a combination of a Galactic bulge component using a triaxial ellipsoidal bar and an NSD component described by a Sérsic model. We use the best fitting model parameters presented in Table 1 of Gallego-Cano et al. (2020) and refer the reader to Section 4 of that paper for a detailed explanation of the fitting.

We convolve and regrid both the star count data and model to match the $36''$ resolution and pixel scaling of the cloud catalog from *Paper III*, as shown in the top three panels of Figure 2. While the model recreates the outer region (i.e. the bulge) quite well, it underestimates the center of the stellar density distribution, as it does not account for the NSC in the central 10 pc . To avoid skewing the NF positions in underestimated modeled regions, we mask out areas where the star count data is greater than the maximum of the model.

Table 1. Summary of posterior fitting results from the PPDFs and LOS distance estimates based on the best-fitting ellipses. The first five columns are taken from Table 1 of Walker et al. (2025). We report the leaf IDs of the cataloged clouds from (clouds with multiple peak velocity features in HNC0 emission are denoted by letters in the leaf ids), the associated cloud names, central coordinates in degrees (ℓ , b), and central velocity from HNC0 (v). From the PPDF fittings (described in Section 3.1) we report the peak relative probability (A), the normalized NF position (d_{NF}), and the 68% confidence interval for the posterior distribution (CI68). We report the estimated LOS distances in front of (-) or behind (+) the GC (LOS pos) obtained from de-projecting the normalized NF positions onto the median x2 orbit, and associated uncertainties (LOS σ) obtained from calculating the standard deviation for the LOS positions of a cloud from each of the three ellipses, as described in Section 4.2. Lastly, we report the estimated galactocentric radii (R_{gal}) and estimated uncertainties based on the projected LOS distances. We report the estimated distances as a qualitative benchmark for the currently available data. The NF distinction methods used for each cloud are noted with a single letter for flux difference (d), flux ratio (r), correlation coefficient (c), star count ratio (s), absorption (a), x-ray distances (x), and estimates from Nogueras-Lara et al. (2026) (k). Colloquial names for catalog clouds are given in the final column. IDs marked with an asterisk denote the largest mask used for clouds with multiple velocity components.

Leaf ID	Cloud Name	ℓ °	b °	v km s ⁻¹	A	d_{NF}	CI68	LOS pos pc	LOS σ pc	R_{gal} pc	R_{gal} σ pc	NF Methods	Colloquial Name
1	G359.475-0.044	-0.525	-0.044	-102.0	2.747	0.404	0.289	-44.1	25.6	72.3	39.8	d,r,c,s	
2	G359.508-0.135	-0.492	-0.135	-56.0	2.433	0.122	0.326	-13.6	17.5	51.1	39.0	d,r,c,s	SgrC
3	G359.561-0.001	-0.439	-0.001	-90.0	3.723	0.168	0.213	-18.6	14.5	49.0	35.1	d,r,c,a,s	
4a*	G359.595-0.223	-0.405	-0.223	-27.0	2.662	0.28	0.298	-30.7	21.7	53.5	30.2	d,r,c,s	
4b	G359.595-0.223	-0.405	-0.223	-20.0	2.314	0.292	0.343	-32.0	23.9	54.4	29.7	d,r,c,s	
5	G359.608+0.018	-0.392	0.018	-78.0	40.092	0.477	0.02	-52.0	17.2	68.1	30.1	d,r,c,a,s	
6a	G359.688-0.132	-0.312	-0.132	-29.0	4.172	0.232	0.19	-25.5	15.7	42.5	23.5	d,r,c,a,s	
6b*	G359.688-0.132	-0.312	-0.132	-21.0	2.451	-0.053	0.348	5.3	15.7	26.5	23.5	d,r,c,a,s	
7a*	G359.701+0.032	-0.299	0.032	-73.0	11.478	0.601	0.058	-65.4	23.0	73.8	20.8	d,r,c,a,s	
7b	G359.701+0.032	-0.299	0.032	-37.0	3.396	-0.223	0.234	23.7	16.9	20.7	22.1	d,r,c,a,s	
8a*	G359.865+0.023	-0.135	0.023	-54.0	2.046	-0.494	0.388	53.0	32.4	7.0	7.5	d,r,c,a	
8b	G359.865+0.023	-0.135	0.023	15.0	2.504	-0.453	0.317	48.5	28.1	7.0	7.6	d,r,a	
8c	G359.865+0.023	-0.135	0.023	62.0	2.982	-0.624	0.266	67.0	31.9	6.8	7.5	d,r,c,a	
9	G359.88-0.081	-0.12	-0.081	15.0	6.111	0.389	0.13	-42.5	18.7	44.7	7.2	d,r,c,a,k	20 km/s
10	G359.979-0.071	-0.021	-0.071	48.0	7.834	0.285	0.101	-31.3	14.0	31.4	1.0	d,r,c,a,k	50 km/s
11a*	G0.014-0.016	0.014	-0.016	-11.0	1.576	-0.649	0.503	69.7	42.3	0.6	0.7	d,r,c,a	
11b	G0.014-0.016	0.014	-0.016	45.0	1.625	-0.658	0.488	70.7	42.0	0.6	0.7	d,r,c,a	
11c	G0.014-0.016	0.014	-0.016	14.0	2.988	-0.508	0.266	54.5	27.9	0.6	0.7	d,r,c,a,s	
12	G0.035+0.032	0.035	0.032	86.0	1.562	-0.689	0.505	74.0	43.7	1.6	1.7	d,r,c,a,s	
13	G0.068-0.076	0.068	-0.076	50.0	6.596	-0.049	0.126	4.9	6.6	4.8	4.5	d,r,c,a,x	Stone
14	G0.105-0.08	0.105	-0.08	53.0	8.681	-0.049	0.091	4.9	5.2	8.0	7.9	d,r,c,a,x	Sticks
15	G0.116+0.003	0.116	0.003	52.0	1.0	-1.107	0.422	119.2	54.6	5.6	5.9	d,r,c,a,s	
16a	G0.143-0.083	0.143	-0.083	-15.0	nan	nan	nan	nan	nan	nan	nan		Straw
16b*	G0.143-0.083	0.143	-0.083	57.0	6.421	0.367	0.123	-40.1	17.7	43.4	9.0	d,r,c,a,s	Straw
17a	G0.255+0.02	0.255	0.02	18.0	10.368	0.724	0.076	-78.6	27.9	84.0	16.5	d,r,c,a,s	Brick
17b*	G0.255+0.02	0.255	0.02	37.0	13.585	0.694	0.058	-75.4	26.2	81.0	16.7	d,r,c,a,s	Brick
17c	G0.255+0.02	0.255	0.02	70.0	4.512	0.638	0.175	-69.4	29.0	75.3	16.4	d,r,c,a,s	Brick
18	G0.327-0.195	0.327	-0.195	16.0	1.983	0.215	0.4	-23.6	23.6	42.5	23.1	d,r,c,s	
19	G0.342+0.06	0.342	0.06	-2.0	39.958	0.769	0.02	-83.5	27.2	92.3	23.7	d,r,c,a,s	B
20	G0.342-0.085	0.342	-0.085	90.0	2.021	-0.326	0.393	34.8	26.8	22.5	23.7	d,r,c,a,s	Sailfish
21a*	G0.379+0.05	0.379	0.05	8.0	20.412	0.616	0.039	-67.0	22.7	79.7	27.7	d,r,c,a,s	C
21b	G0.379+0.05	0.379	0.05	39.0	4.059	0.575	0.186	-62.5	27.3	75.9	26.8	d,r,c,a,s	D
22	G0.413+0.048	0.413	0.048	19.0	40.109	0.845	0.02	-91.7	29.8	103.2	29.2	d,r,c,a,s	E/F
23	G0.488+0.008	0.488	0.008	28.0	6.223	0.684	0.127	-74.3	28.6	92.5	35.9	d,r,c,a,s	
24	G0.645+0.03	0.645	0.03	53.0	11.963	0.471	0.059	-51.3	18.6	86.8	52.5	d,r,c,a,s	

25	G0.666-0.028	0.666	-0.028	62.0	4.328	0.213	0.183	-23.4	14.8	71.8	55.6	d,r,c,a,s	Sgr B2
26a*	G0.716-0.09	0.716	-0.09	28.0	3.631	0.161	0.224	-17.8	14.7	73.5	60.2	d,r,c,s	G0.714
26b	G0.716-0.09	0.716	-0.09	58.0	9.443	0.025	0.083	-3.1	4.4	66.8	63.8	d,r,c,s	
27	G0.816-0.185	0.816	-0.185	39.0	9.698	-0.06	0.082	6.0	5.2	72.4	72.7	d,r,c,s	
28a	G0.888-0.044	0.888	-0.044	14.0	14.373	-0.049	0.055	4.9	3.7	79.4	79.8	d,r,c,s	
28b	G0.888-0.044	0.888	-0.044	26.0	14.373	-0.049	0.055	4.9	3.7	79.4	79.8	d,r,c,s	
28c*	G0.888-0.044	0.888	-0.044	84.0	14.907	-0.037	0.053	3.6	3.3	79.9	80.0	d,r,c,s	
29a	G1.075-0.049	1.075	-0.049	74.0	1.698	0.02	0.467	-2.6	19.7	99.6	91.3	d,r,c,s	
29b*	G1.075-0.049	1.075	-0.049	85.0	6.49	-0.002	0.122	-0.3	5.0	98.6	96.6	d,r,c,s	
30a*	G1.601+0.012	1.601	0.012	48.0	24.036	-0.065	0.033	6.6	3.4	144.6	145.8	d,r,c,s	G1.602
30b	G1.601+0.012	1.601	0.012	58.0	18.226	-0.072	0.043	7.4	4.1	144.3	145.6	d,r,c,s	G1.602
31	G1.652-0.052	1.652	-0.052	50.0	19.485	-0.039	0.041	3.8	2.8	150.4	150.8	d,r,c,s	G1.651

The catalog cloud masks are then applied to the data and model maps. For each mask, we take the pixel-wise ratio of the star count data and the model. The cloud masks contain anywhere between $\sim 8 - 400$ pixels. To ensure at least 3 pixels per mask, we exclude cloud masks which contain $> 20\%$ of masked pixels from the analysis, resulting in 9 excluded cloud IDs: 8a, 8b, 9: 20 km/s, 10: 50 km/s, 11a, 11b, 13: Stone, 14: Sticks.

A visual summary of the star count ratio method is shown in Figure 2. From top to bottom the panels show: (i) Herschel column density map with contours and ID numbers corresponding to the catalog presented in *Paper III* and summarized in Table 1, (ii) stellar density map from Nishiyama et al. (2013), (iii) modeled star count map from Gallego-Cano et al. (2020) convolved and regrid to match the $36''$ column density map, (iv) cutout of star counts for the molecular clouds, (v) cutout of modeled star counts, and (vi) ratio of the star count map to the model map, normalized to the near/far scaling used in the Bayesian synthesis (See Section 3.1). White areas in panels (i)–(iii) indicate masked pixels where the star count is greater than the maximum of the model. The blue and red color scale in panel (iv) denotes likely near or far side positions, respectively. The black star denotes the location of SgrA*.

The median star count ratio within each mask is used as the overall NF result for a given cloud. The star count ratios are ultimately normalized on a 1 (near) to -1 (far) scale, and folded in to the Bayesian synthesis method described in Section 3.1.

2.4. Distance Constraints from X-rays

Two objects in the catalog, the Stone (ID 13) and Sticks (ID 14) clouds, have distance constraints determined by detections of Fe K_α emission from reflected X-rays (Clavel et al. 2013; Chuard et al. 2018; Marin et al. 2023; Stel et al. 2025). Sunyaev & Churazov (1998)

presents a method for calculating projected line-of-sight distance estimates from the Fe line emission based on the age of a flaring event responsible for the illumination. These calculations provide tight distance constraints on illuminated objects, as it is impossible for illumination to occur without intersecting with the path of the event sweeping out from the central source. SgrA* is often assumed as the source for both a single and two-flaring event scenario due to the energy required to explain the observed emission (Clavel et al. 2013). Clavel et al. (2013); Chuard et al. (2018) and Stel et al. (2025) use this method to determine the distances of the clouds to be between 5-25 pc behind SgrA*. Additionally, Marin et al. (2023) perform polarization measurements of the reflected X-ray emission to constrain the age of a single flaring event to be 205_{-30}^{+50} yr, and assumptions of two flaring events imply ages of 100 yr and 200 yr. Assuming a 200 year old event results in a possible range in line-of-sight distances for both clouds within 30 pc behind the GC and 20 pc (10 pc) in front for the Stone (Sticks) cloud. We use this range as an added constraint on the NF distance estimates for the Sticks and Stone clouds.

2.5. Distance constraints from Stellar Kinematics

Distance estimates from stellar density maps are possible to obtain for some clouds in the CMZ. Nogueras-Lara et al. (2026) report distance estimates for the 20km s^{-1} and 50km s^{-1} Clouds (IDs 9 and 10, respectively), based on proper motions estimated from their observed color magnitude. The proper motion measurements were compared with the Galactocentric velocity profile to obtain a distance. This analysis places the 50km s^{-1} and 20km s^{-1} clouds at 43 ± 8 pc and 56 ± 11 pc in front of SgrA*, respectively. We include these distance estimates in our analysis.

3. BAYESIAN SYNTHESIS AND ORBITAL FITTING

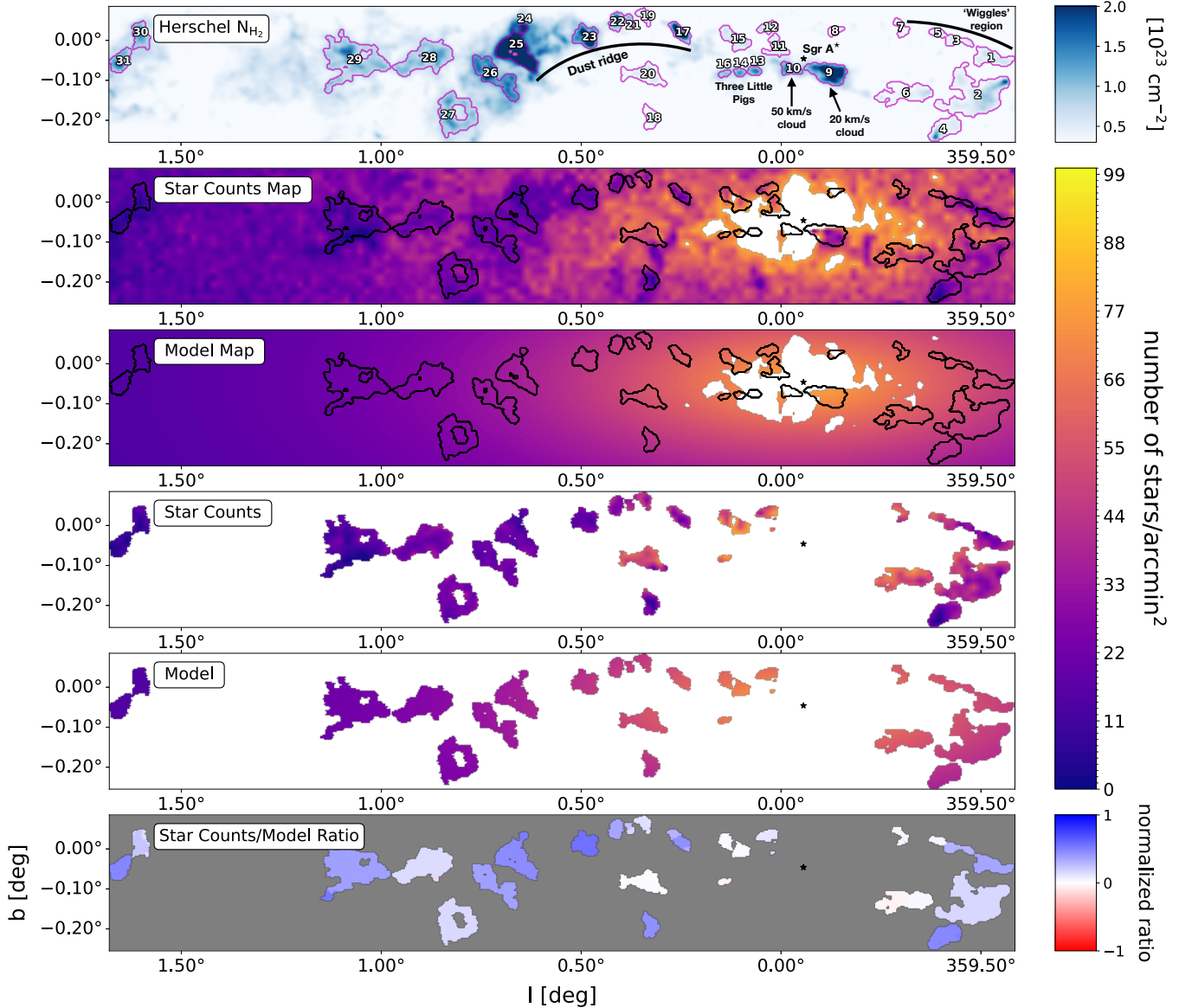


Figure 2. Stellar density maps of the CMZ show dark extinction features that can be used to calculate a star count ratio to determine NF positions of molecular clouds in the catalog. From top to bottom, the panels show: (i) Herschel column density map with black contours and ID numbers correspond to cloud masks summarized in Table 1, (ii) stellar density map from Nishiyama et al. (2013) and (iii) modeled star count map from Gallego-Cano et al. (2020), both of which we convolve and regrid to match the $36''$ Herschel column density map. White areas are masked pixels where the star count is greater than the maximum of the model. Panel (iv) is a cutout of star counts for the molecular clouds; panel (v) is a cutout of modeled star counts; and panel (vi) is a ratio of the star counts to the model map. The blue and red color scales denote more likely near or far side positions, respectively. Clouds containing $> 20\%$ of masked pixels are excluded from analysis. The black star indicates the location of SgrA*.

3.1. Bayesian synthesis of near/far methods

We present an automated Bayesian framework to combine information from multiple datasets into a posterior distribution of a cloud’s likely NF position in the CMZ. We set up the method to synthesize data with the goal of adding future datasets and results, in order to further constrain the posteriors and subsequent orbital fitting.

Our approach is inspired by Ellsworth-Bowers et al. (2013, 2015), who employed a Bayesian approach to produce distance probability density functions (DPDFs) for

Table 2. Summary of normalization parameters and weights for each near/far distinction method.

Method	max	min	Gaussian σ	weight
Flux Difference	150 MJy/sr	-150 MJy/sr	normalized σ_{MAD} for each source	1
Flux Ratio	1	0	normalized σ_{MAD} for each source	1
Correlation Coefficient	1	-1	based on stdv of dataset	2
Absorption	2	0	normalized error for each source	2
Star Count Ratio	2	0	$3 \times$ median σ_{MAD} for the entire sample	1
X-ray (IDs 13, 14)	150 pc	-150 pc	-	2
Nogueras et al. (2026) (IDs 9, 10)	150 pc	-150 pc	normalized uncertainties for each source	2

constraining distances to infrared dark clouds in the Galactic disk. The authors introduce Galactic rotation curves as a likelihood function, which is subject to ambiguity in projected orbital motions, and use various ancillary datasets as priors to constrain distance estimates (see [Ellsworth-Bowers et al. 2013](#)). Similarly, the dense molecular clouds in the CMZ are subject to ambiguity in their line-of-sight locations relative to the GC, making the DPDF approach a promising starting point for developing constraints on cloud positions.

Distinguishing line of sight distances to infrared dark clouds in the Galactic disk has previously been achieved by comparing emission column densities to column densities calculated via MIR extinction ([Ellsworth-Bowers et al. 2013, 2015](#)), or from stellar extinction using precise estimates from Gaia (e.g. [Edenhofer et al. 2024; Zhang et al. 2025](#)). However, *Paper IV* showed that MIR extinction in the CMZ is quickly saturated due to the extreme column densities, making obtaining line of sight distances to molecular clouds difficult with currently available data. While recent studies of stellar kinematics can distinguish between near and far positions in the CMZ (e.g. [Nogueras-Lara et al. 2026](#)), this has only been obtained for a couple targets. Thus, rather than extracting distances for CMZ clouds, we use Bayes' Theorem to obtain a *position* PDF (hereafter PPDF), which gives the distribution of a cloud's NF position relative to SgrA*. We define the PPDF as a function of near-far position (p_{NF}) by

$$\text{PPDF}(p_{NF}) = \mathcal{L}(p_{NF}) \prod_i P_i(p_{NF}), \quad (1)$$

where $\mathcal{L}(p_{NF})$ is a likelihood function and $P_i(p_{NF})$ are prior PPDFs based on ancillary datasets. We use the median $8\mu\text{m}$ flux difference as the basis for our likelihood function, as it provides the simplest comparison between the Spitzer $8\mu\text{m}$ emission and model background. PDF distributions from the other methods are treated as priors to constrain the NF estimates. The posterior PPDF is then defined as the product of the likelihood function

with the priors, normalized to unit total probability, i.e. $\int_0^{\text{inf}} \text{PPDF}(p_{NF}) d(p_{NF}) = 1$.

Before constructing the likelihood function and prior positional distributions, we map each of the NF position measures to the same quantitative scale of -1 (far) to +1 (near) using a min-max normalization procedure:

$$z(x) = 2 \left(x - \frac{\text{min}}{\text{max} - \text{min}} \right) - 1, \quad (2)$$

where z is the normalized value of a given data value x for each dataset (see Appendix C, Table 4 for the unnormalized values used to build the priors for each method). The normalization is determined by chosen minimum and maximum limits for each method, reported in Table 2. The min-max scaling is applied such that $z = 0$ corresponds to the threshold between NF distinctions.

Similarly, the uncertainties (σ) for each method are normalized using the same min and max values, such that the normalized σ is scaled from 0; i.e. $\sigma_{\text{norm}} = |z(\sigma) - z(0)|$. This scaling is analogous to calculating the uncertainty of the normalized dataset distribution.

After the data have been normalized, we model the shape of each method's NF distribution for a given cloud as a 1-D Gaussian of the form:

$$P(x) = A \cdot \exp \left(\frac{-(x - \mu)^2}{2\sigma^2} \right), \quad (3)$$

with relative probability $P(x)$ which peaks at value A . The offset μ corresponds to the normalized NF position ($z(x)$), and the width of the distribution, σ , is set by the normalized uncertainty ($z(\sigma)$). Each method's distribution is normalized to integral unit probability.

The choice to model the priors as Gaussian was made to flexibly represent the overall distribution for each cloud. The normalized distributions for most methods appear relatively Gaussian or log-normal. Additionally, most methods report a likely NF position with some uncertainty, which is easily represented with a Gaussian formalism. We highlight a few examples of the normalized distributions for different methods compared to

Gaussian priors with various uncertainty estimations in Section A. The Bayesian framework presented here is intended to be adjustable, such that other researchers may opt for different distribution shapes.

Finally, we assign a weight to each method based on the relative confidence in the methods' NF position estimates. The weights of the available datasets for each source are totaled and then individual weights rescaled to be used in the Bayesian combination.

Both the construction of prior distributions and the weighting prescription are flexible, allowing for any researcher to determine relative confidence in any combination of datasets. Altering the weights will impact the relative probability (i.e. the Gaussian A variable) of each prior distribution, and can influence the overall posterior distributions depending on which method is given higher confidence. Thus, the weighting of each method must be justified on an individual basis.

We discuss the normalization parameters used to build prior Gaussian distributions, and weighting justifications for each method below. The parameters are summarized in Table 2.

Flux difference: To build the Gaussian priors, we must obtain normalized uncertainties (σ) and offsets (μ), which for the $8\mu\text{m}$ flux difference correspond to the σ_{MAD} and median flux difference values for each cloud.

The $8\mu\text{m}$ flux difference method defines the threshold between near and far positions as the central flux value in the variable CMZ minus the constant $8\mu\text{m}$ foreground emission (f), i.e. $\Delta F_{\text{center}} = \frac{\text{CMZ}}{2} - f \approx -108 \text{ MJy/sr}$. More positive (negative) values denote more likely near-sided (far-sided) positions. To normalize the median flux difference values to a -1 (far) to +1 (near) scale, we use Equation 2 with min and max extents of -150 MJy/sr and 150 MJy/sr, respectively. The asymmetric min and max bounds about ΔF_{center} are a consequence of the assumed foreground, which is taken as the averaged minimum intensity of the Brick and Sgr B2. The flux difference is thus a quantitative measure of extinction relative to this value. The overall sample distribution is approximately Gaussian, offset by the value of ΔF_{center} . This offset NF threshold of -108 MJy/sr has a normalized value of -0.72, which is subtracted from the normalized μ values such that $z = 0$ corresponds to the -108 MJy/sr.

The Gaussian σ for the flux difference is set by the normalized median absolute deviation (σ_{MAD}) of the flux difference distribution for each cloud in the catalog, obtained using Equation 2.

Lastly, we assign the flux difference a relative weighting of 1, as there are significant uncertainties pertaining to assumptions for modeling constant foreground and

background emission.

Flux ratio: The $8\mu\text{m}$ flux ratio method from *Paper IV* is defined such that a value of 1 denotes an exact match to the $8\mu\text{m}$ background, a value of 0 denotes complete obscuring of the background by a near-sided cloud, and the threshold between near and far is equal to 0.5. Because the flux ratio has clearly defined bounds for NF positions, we use the minimum and maximum of the flux ratio dataset to define the limits for Equation 2.

The uncertainty for the flux ratio are determined from the normalized σ_{MAD} for each cloud using Equation 2.

Similar to the flux difference method, we assign the flux ratio a relative weighting of 1, as it is subject to the same uncertainties from modeling the constant foreground and background emission.

Correlation coefficient: By definition, the Pearson correlation coefficient, r , is bound between -1 (anti-correlation) and +1 (1:1 correlation) (Pearson & Galton 1895). *Paper IV* defines masks where $r \geq 0.3$ as near-sided. For $|r| \geq 0.3$, we assign a Gaussian uncertainty equal to the standard deviation of all correlation coefficient values in the dataset.

The range between $-0.3 < r < 0.3$ is an ambiguous distinction, that requires more information to discern the NF position. Many astrophysical studies assume $|r| < 0.4$ as a weak or poor correlation (e.g. Mokeddem et al. 2026; Aizawa et al. 2025). We assign clouds with notably weak correlation a larger uncertainty, as results in this range cannot confidently indicate either near or far-sided positions. For clouds within these ranges, we assign a normalized uncertainty to be 3 times the standard deviation of all values in the dataset, i.e. $\sigma_r = 3 \cdot \text{stdv}(r)$

The uncertainties and assumptions for the background estimates needed to compute the extinction column densities differ from those used for the $8\mu\text{m}$ methods. Since the correlation coefficient is based off of the statistical correlation of column densities for each pixel in the cloud mask, we determine it a more confident measure of NF distinction, and assign a relative weight of 2.

Molecular line absorption: Line absorption fractions from *Paper III* are defined such that fractional absorption values > 1 indicate a far-sided position, and values < 1 indicate a near-sided position. We normalize the absorption data using a minimum value of 0 and maximum value of 2.

Uncertainties for the absorption method are obtained by calculating the error of the individual fractional absorption maps. For a given cloud mask, the fractional

absorption is calculated using via: (median GBT C-Band Continuum + a cosmic microwave background estimate) / abs(H₂CO Min Intensity). For the C-band continuum, we estimate the noise as the standard deviation of the C-band map of the cloud mask (σ_{GBT}). For the H₂CO uncertainty, we use the signal-to-noise ratio (SNR_{H₂CO}) of the masked H₂CO data relative to the RMS of the cube. The absorption uncertainty σ_{absorp} for the cloud is then calculated via:

$$\sigma_{\text{absorp}} = \left(\frac{\sigma_{\text{GBT}}}{\text{SNR}_{\text{H}_2\text{CO}}} \right) \sqrt{\left(\frac{\sigma_{\text{GBT}}}{\text{med GBT}} \right)^2 + \left(\frac{\text{SNR}_{\text{H}_2\text{CO}}}{\text{min H}_2\text{CO}} \right)^2} \quad (4)$$

The molecular line absorption method is assigned a relative confidence weight of 2, based on the strong absorption features seen in the H₂CO spectra.

We note that two cloud IDs 9 (20 km/s cloud) and 25 (SgrB2) have high fractional absorption, however their NF distinctions were manually overruled in *Paper III* due to embedded star formation confusing the absorption analysis. These two clouds are also excluded from the absorption dataset for the PPDF analysis.

Star count ratio: The star count ratio is defined such that values > 1 indicate a far-sided position, where the star count exceeds the model; and values < 1 indicate a near-sided position, where the star count is less than the expected stellar distribution model. We normalize the star count ratio using a minimum value of 0 and maximum value of 2.

The largest uncertainty in the star count method is due to the modeled stellar distribution. We assign a common normalized Gaussian σ of 3 times the median σ_{MAD} of the normalized data obtained using Equation 2. Similar to the 8 μm methods, we assign a relative weight of 1 to the prior distributions, due to the large uncertainties from background modeling.

X-ray echoes: Unlike the other NF distinction methods, X-ray echoes provide a range of line of sight distance estimates for illuminated objects based on a given age of the illuminating event. The near-side distance constraints for the Sticks and Stone clouds from X-rays are quite stringent. Positions closer than 20 pc in front of the GC would reduce the delay between the past illumination and its reverberation in the cloud, so the event responsible for the echoes would have been detected directly by X-ray telescopes, which is not the case. The far-side limit is less constrained due to uncertainties in the age and number of events. Current estimates place the clouds up to 30 pc behind the GC (e.g Clavel et al. 2013; Chuard et al. 2018; Stel et al. 2025). It is pos-

sible for the clouds to lie anywhere within this range, but unlikely elsewhere. Thus, we characterize the X-ray distance constraints as a flat top-hat function, rather than a Gaussian curve or a piece-wise combination of a flat-top with broadened Gaussian tails.

As with the previous data sets, we convert the top-hat function to the -1 to +1 scaling. Normalizing the LOS distances onto a NF scaling requires a way to compare the distances to the relative positions of the clouds for which true distance estimates are unavailable. At this step in the procedure, there is no direct way to compare the reported distances and NF values. However, we may introduce an prior assumption for the minimum and maximum values along the LOS by projecting the the distances onto an orbital ring of an assumed radius. We use a 150 pc galactocentric radius as a standard assumption for the CMZ radius, similar to other orbital model predictions in the literature (e.g. Kruijssen et al. 2015; Sofue et al. 2025). The ± 150 pc estimate is used as the maximum and minimum values for Equation 2. The top-hat function is then normalized to integral unity and treated as a PDF for the Bayesian combination.

The initial assumption for the CMZ radius has a non-negligible impact on the NF scaling, as it will place the cloud closer or further from the center of the ring (see Section 6.1 for a detailed discussion of uncertainties).

Since the X-ray distances are well-constrained, and provide some of the more confident measures for line-of-sight (LOS) positions of clouds, we assign the method a relative weighting of 2.

Distances from proper motions: The estimated distances to the 20 and 50km s⁻¹ clouds from Nogueras-Lara et al. (2026) are converted to the -1 to 1 NF scaling similar to the X-ray distance constraints, using ± 150 pc as the maximum and minimum values for Equation 2. However, we model the prior distributions as Gaussian, scaling the associated uncertainties as done when constructing the other Gaussian priors.

Similar to the X-ray methods, converting the LOS distances to NF scaling requires an initial assumption of a CMZ radius. Altering this value will impact the normalization for this method, placing the clouds closer or further from SgrA* depending on the chosen radius.

We assign a relative weight of 2 to the priors created from this method. Priors for both the stellar kinematics and X-rays are have significant systematics associated with projecting the LOS distances onto an assumed orbital radius (See Section 6 for detailed discussion of uncertainties). The LOS distance-related metrics still provide useful limitations for the relative NF positions of these clouds, which is especially useful when inter-

preting the region near SgrA*. We choose to include the x-ray and stellar kinematics methods in this analysis for a preliminary estimation of their positions, which may be further constrained in future iterations.

After combining the priors, the posterior PPDF is normalized to unit integral probability. Examples of normalized prior distributions for each method, as well as the normalized posterior distributions are shown in Figures 3 and B.1 as colored and black lines, respectively. The location of the posterior peak on the x-axis (d_{NF}) indicates the most likely, normalized NF position of the cloud. The peak value (A) gives the relative probability of the cloud being located at that NF position. We also report a 68% confidence interval (CI68) for each posterior PPDF, which will be used as uncertainties in the orbital fitting procedure in Section 3.2.

3.2. Minimization procedure to find a best fitting x_2 ellipse

Material in the CMZ is thought to lie on a closed ellipse, often treated as x_2 orbits which arise from the Galactic bar potential as described by numerical solutions derived in Binney et al. (1991). It is not fully understood what sets the extents of the x_2 orbits, though there is evidence that the sizes are correlated to the location of Inner Linblad Resonances of the Galactic potential (e.g. Contopoulos & Grosbol 1989; Athanassoula 1992; Buta & Combes 1996). A simple parametric definition of an x_2 ellipse can be described in cartesian coordinates as follows:

$$x = a \cos(\phi) \quad (5)$$

$$y = -b \sin(\phi) \quad (6)$$

$$z = z_0 \sin(-2\phi + \alpha) \quad (7)$$

with radii determined by semi-major axis a and semi-minor axis b . The vertical height of the orbit is determined by z_0 . The sinusoidal term of the z component includes a factor of -2, which makes the ellipse appear as the twisted infinity shape in a plane-of-sky lb projection (note this implies that the vertical oscillation frequency is a multiple of the orbital period, which is unlikely, though we use it here to test a simple geometry). The azimuthal angle ϕ is measured from the starting point of the ellipse, and α is a phase offset. This modeled ellipse assumes a constant angular momentum (i.e. $L_z = v_\phi R$ is a constant), and allows for vertical oscillations. The assumption of constant angular momentum, although not exact, is a reasonable approximation for x_2 orbits and the PPV shape of the observed gas distribution (see Paper III). Our assumptions differ from the closed ellipse proposed by Molinari et al. (2011) in

two ways: 1) we center the ellipse on SgrA* (i.e. the minimum of the gravitational potential) while theirs is not, and 2) we assume a constant angular momentum, while Molinari et al. (2011) assumes constant orbital velocity. A constant angular momentum allows for higher (lower) velocities at peri(apo) center, and more closely resembles a true x_2 orbit (e.g. see Levy 2022).

We examine the parameter space for the standard parametric ellipse by projecting the equations into a LOS derived geometry, such that we fit the ellipse as it is seen in lbv space. We fit using the following parameters: a , b , and z_0 to describe the size of the ellipse; the initial tangential velocity (v_0); the angle of the ellipse measured from the Sun-Galactic center line (θ); and phase angle α . In Paper III, the parameters of the toy model were chosen by-eye to match the observed lbv gas distribution, and resulted in reasonable fits to NF positions determined by the molecular line analysis in Paper III and the dust extinction analysis in Paper IV.

To find a best fitting x_2 orbital model, we employ a minimization routine that incorporates the normalized posterior distributions for each source obtained in Section 3.1, and the x_2 ellipse model defined above.

We use the Non-Linear Least-Squares Minimization and Curve-Fitting python package `lmfit` (Newville et al. 2025) as a framework for our orbital fitting procedure. The `lmfit.minimize()` function performs standard χ^2 minimization, and provides a flexible framework to adjust parameters and fitting methods. We use a Nelder-Mead fitting method, which tends to more accurately and efficiently sample the available parameter space compared to a least-squares regression (Kumar 2023).

The target of the minimization procedure is a residual function of a given modeled ellipse to the dataset of posterior PPDFs. The procedure is as follows:

1. We initialize an elliptical orbital model based the parametric equations 5-7. The ellipse function takes parameters of a semi-major axis (a), semi-minor axis (b), orbital height (z_0), initial tangential velocity (v_0), a rotation about the z-axis (θ), and phase angle (α).
2. In order to compare the initialized orbital model with the likely NF cloud distributions, we must first provide a NF model estimate. We follow a similar normalization procedure as described in Section 3.1 to translate the model's l , b , and v position arrays onto the -1 (far) to +1 (near) scaling. We perform the scaling procedure using Equation 2, where the min and max values for normalization are based on limits of observed lbv projections of the CMZ ring: $(\ell_{min}, \ell_{max}) = (-0.6^\circ,$

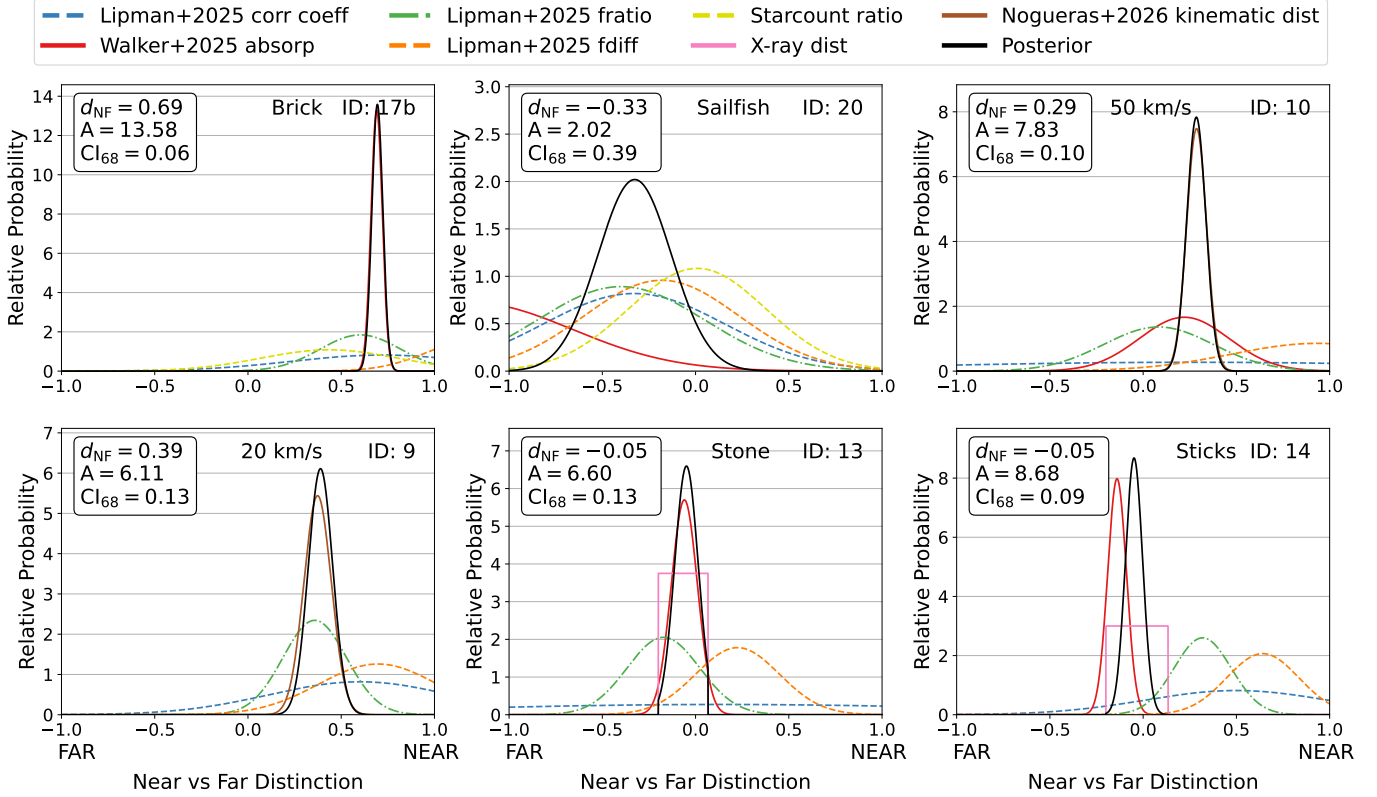


Figure 3. The methods used to infer NF positions of individual clouds in the CMZ can be combined in a Bayesian framework to create a posterior distribution of NF likely positions for a given cloud on a normalized scale of -1 (far) to +1 (near). The flux difference (orange dashed line) is used as a likelihood function, and is multiplied by distributions for the flux ratio (green), correlation coefficient (blue), absorption fraction (red), and star count ratios (yellow). A handful of clouds have prior data from X-rays (pink), or stellar kinematics (brown). After taking the product of the priors, we report the location of the peak (μ), the relative probability peak (A), and the 68% confidence interval (CI_{68}), which are used to obtain a Positional PDF posterior distribution (PPDF; black solid line). The peak of the posterior indicates the most likely NF position of the cloud. All distributions are normalized to unit integral probability.

- 1.7°); (b_{min}, b_{max}) = (-0.3°, 0.1°); and (v_{min}, v_{max}) = (-100 km/s, 100 km/s). The central lbv positions for each catalog cloud are normalized using the same limits.
3. Next, we find the minimum distance between each cloud in the catalog and the model ring using the `scipy.cdists` package with a Mahalanobis distance metric (Mahalanobis 1936, also see e.g. Blaylock-Squibbs & Parker (2023)). The Mahalanobis distance measures the distance between the model and the data, normalized by the data uncertainty.
 4. Due to the tight correlation of points in lbv space, the Mahalanobis distance alone fails to constrain the latitude distribution of observed material. To address this, we employ a Wasserstein distance metric (Monge 1781), also referred to as the “earth mover’s distance” in computer science and optimal transport problems (see Kantorovich 1942; Villani

2021). The Wasserstein distance is a measure of similarity between two probability distributions, and can be written as:

$$W_p(P, Q) := \inf_{\pi \in \Gamma(P, Q)} \left(\int_{\mathbb{R} \times \mathbb{R}} \|x - y\|^p d\pi(x, y) \right)^{1/p} \quad (8)$$

Where P and Q are probability distributions on \mathbb{R} with p moments. The 1D Wasserstein distance computes the distance between probability distributions, and quantifies the “cost” of moving points from the model to the observed data (in the earth mover’s context, the physical metric of work needed to convert one pile of dirt to another). The cost is calculated as the product of the probability mass to be transported and the distance the mass is moved. For our purposes, we sample the ellipse model’s latitude distribution by the number of data points used in the model fitting (22), and then uniformly distribute the total catalog cloud

mass along the latitude of the model. We then evaluate the cost to move the mass on the ellipse to match the data, and vice versa. The sum of the transportation costs for each cloud is returned as a scalar. We add this output scalar to each of the minimum Mahalanobis distances for a given cloud, resulting in an optimized distance which corrects for the observed latitude-distribution of the data.

5. Using the model point with the minimum Mahalanobis distance to the cloud, we assess the model and cloud’s NF agreement using a k-nearest neighbors approach with the `scikit-learn` package’s `NearestNeighbors` functionality. We use $k = \sqrt{N} = 600$, where N is the number of data points in the model. The NF positions of the nearest neighbors are compiled, and the most common NF position value is used for the nearest model point, $d_{\text{NF,model}}$. This step is most important near the edges of ellipse model, where the nearest neighbors may span between the near and far sides.

6. We then calculate a residual penalty between the NF position of the nearest *lbv* point on the ellipse to the posterior likelihood distribution for the cloud. We approximate each cloud’s PPDF as a Gaussian distribution which gives the relative probability that the cloud lies at a given distance, $P(d)$:

$$P(d) = A \cdot \exp\left(\frac{-(d - d_{\text{NF}})^2}{2(\text{CI68})^2}\right), \quad (9)$$

where A , d_{NF} , and CI68 are the peak probability, most likely NF position, and CI68 of a given cloud as reported in Table 1. Using the above formalism, which utilizes the full shape of the Gaussian PPDF, we find the relative probability that a cloud exists at the *lbv* location of the nearest model point ($P(d_{\text{NF,model}})$). We then find the difference between the model point’s relative probability and the peak probability of the cloud at its most likely position from the PPDF ($P(d_{\text{NF}}) = A$). Thus, we compare relative probabilities of the model position to the peak PPDF value. This difference quantifies how far the closest NF point on the ellipse model is from a cloud’s PPDF peak. The result is treated as a NF penalty value.

7. Finally, each cloud’s optimized distance to the model (Mahalanobis distance + Wasserstein output scalar) and NF penalty are added together to create a list of residuals for the input fitting model. The calculated reduced chi-square, χ_{red}^2 , is used to determine the best fit to the dataset.

3.2.1. Points excluded from orbital fitting

While the cloud catalog provides a list of the densest structures in the CMZ, not all reported structures are necessarily appropriate to include in the x_2 orbital fitting. The full catalog has a total of 47 objects, including 17 sub-masks for clouds with multiple velocity components detected in the molecular line data. To avoid artificially weighting these multi-component sources over the single-component clouds, we only include the masks containing the most pixels for clouds with multiple velocity components. The IDs relating to the main masks used in the fitting are noted by an asterisk in Table 1.

Additionally, we only include clouds that could be reasonably associated with the main CMZ orbit, and have sufficient data to inform the fitting. Cloud IDs 27 and greater lie off of the typically assumed 100 pc projected radius. These clouds also lack data from the absorption method, and show the most conflict between the dust extinction methods. We exclude these clouds from the fitting based on the inconsistencies between methods and lack of data in these regions.

Lastly, there are a handful of clouds near SgrA* in projection that likely do not lie on a typical x_2 orbit, but perhaps sit closer to SgrA* or the CND. The 20 and 50 km/s clouds (IDs 9 and 10, respectively) have been theorized to be interacting with or falling in towards the CND based on their line of sight velocities (Lee et al. 2008; Karlsson et al. 2003; Yan et al. 2017). Likewise, the Stone (ID 13) and Sticks (ID 14) clouds, have been confidently constrained to be near SgrA* via X-ray fluorescence, as discussed above (Clavel et al. 2013; Chuard et al. 2018; Stel et al. 2025; Marin et al. 2023). Enough evidence points towards these four clouds not being a part of the main x_2 orbit that the majority of other structures seem to trace. Including clouds which do not lie on x_2 orbital paths into the minimization procedure can skew the fitting and greatly impact the potential best-fit CMZ sizes. The impact is especially important for these clouds, which have well-constrained PPDFs. Thus, we remove IDs 9, 10, 13, and 14 from the orbital fitting procedure and instead use the fitting results to interpret their relative positions to other clouds based on their posterior PPDFs in Section 5.

4. RESULTS

4.1. Synthesis of Near vs Far Positions for CMZ Catalog Clouds

The posterior PPDFs described in Section 3.1 peak at the location of the most likely NF position for each cloud, and are measures of the relative NF positions of clouds between each other. We report the posterior PPDF parameters in Table 1. The PPDF peak A repre-

sents the relative probability of the cloud being located at a given position. The d_{NF} value indicates the normalized NF position and CI68 is the 68% confidence interval of the highest peak of the posterior distribution.

In many cases, the absorption has a significant impact on the position and uncertainty of the posterior due to the more constrained uncertainties (e.g. IDs 17b, 13, and 14 in Fig 3). The posterior PPDFs are mostly Gaussian, although there are some distributions which show double peaks (e.g. ID 15) or sharp edges due to the step-function priors for X-ray data (e.g. ID 13). Overall, the Bayesian combination results in reasonable distributions, given the available constraints, and can be used to confidently determine relative positions of the cataloged clouds.

4.2. Best fitting x_2 orbits

The fitting procedure described in Section 3.2 outputs parameters of a semi-major axis (a) in kpc, semi-minor axis (b) in kpc, orbital height (z_0) in kpc, initial tangential velocity (v_0) in km s^{-1} , a rotation about the z-axis (θ) in degrees, and phase offset of the ellipse α in radians. During initial tests, the fitting algorithm produced various CMZ sizes depending on the initial conditions, particularly the input a and b radii, which are well-correlated.

To find convergent values for each of the parameters, we run the fitting procedure for a grid of initial ellipse sizes with major axes ranging from 10 – 300 pc in 5 pc increments. The input minor axis is set using the initial b/a ratio from the *Paper III* ellipse ($b/a = 0.61$). Using elliptical initial values avoids cases where the algorithm may sample minor axes larger than the major axes. We do not explore the parameter space of initial conditions

for z , v_0 , θ , or α as we are most interested in the possible CMZ sizes, and find these values from *Paper III* to be reasonable initial guesses for the fitting procedure. Additionally, there are degeneracies in the projections from θ and α , meaning it is more efficient to open a broad parameter space for these variables to sample in the optimization, rather than vary them in the parameter grid. After setting the input values, the minimization routine searches for ellipse parameters between set lower and upper bounds, reported in the first two columns of Table 3, without further constraints. The output distribution of the parameter grid test is shown in Figure 4. The gray shaded region in the left column covers the χ_{red}^2 range $1 < \chi_{\text{red}}^2 < 3$ where a majority of the outputs converge. Cyan (magenta) points correspond to outputs for ellipses with a major axis greater (less) than the median a_{out} value. Gray points are outputs with $\chi_{\text{red}}^2 > 3$. The right column shows histogram distributions of the points between $1 < \chi_{\text{red}}^2 < 3$, with a gold line denoting the median value of each output parameter.

The parameter grid results in fits that are within χ_{red}^2 ranges of $2.4 < \chi_{\text{red}}^2 < 3.5$, with $\chi_{\text{red}}^2 = 3$ used as a typical indicator for reasonable fits. The best convergence for each parameter seems to fall within the range of $2.4 < \chi_{\text{red}}^2 < 3.0$. We find the minimum, median, and maximum value of each output parameter value based on a ranges where the χ_{red}^2 converged for the grid. We assume the median fit value as the best-fit for the parameter search, though the bulk gas may exist on orbits anywhere between the inner and outer extents. We summarize the outputs from the grid search in Table 3. The smallest semi-major axis obtained within the convergent χ_{red}^2 range is $a = 60$ pc and the largest is $a = 296$ pc.

Table 3. Summary of the upper and lower bounds used for the orbital ellipse minimization routine, example parameters from Paper III, and the output fitted parameters obtained from the parameter grid search. The ellipse function takes parameters of a semi-major axis (a), semi-minor axis (b), orbital height (z_0), initial tangential velocity (v_0), position angle of the semi-major axis with respect to the line-of-sight (θ), and phase offset of the ellipse (α). The input parameters for a and b are set by a ratio ($b/a = 0.61$) using parameter grid sampling inputs between $10 < a < 300$ pc in 5 pc increments. All other inputs match those in *Paper III*. We report the median parameter values from the parameter grid evaluation for results with $1 < \chi_{\text{red}}^2 < 3$. The median output fit values from the parameter grid search are taken as the best-fitting parameters for an average orbit. The inner and outer extent values are used to create the top-down projection in Fig 6.

Fitting parameter	Input Parameters			Parameter Grid Search				Top-Down Extents	
	Lower Bound	Upper Bound	Value from Paper III	Min Fit Value	Median Fit Value	Max Fit Value	Standard Deviation	Inner Extent	Outer Extent
a [kpc]	0.01	0.3	0.9	0.060	0.083	0.296	0.066	0.072	0.146
b [kpc]	0.01	0.2	0.055	0.018	0.034	0.098	0.022	0.026	0.058
z_0 [kpc]	0	0.05	0.0125	0.0123	0.0140	0.0198	0.0014	0.0146	0.0144
v_0 [km/s]	75	175	130	75.0	129.6	170.8	25.3	130.9	109.0
θ [deg]	-180	180	25	10.0	16.6	82.3	25.1	15.8	42.9
α [rad]	$-\pi/2$	$\pi/2$	0.4	-1.08	0.12	1.57	0.66	0.04	0.11

Most of the parameter grid test converged on a median value of $a = 83$ pc. We also report the average values from the parameter grids for output with major axis values above and below the median $a = a_{\text{median}}$, corresponding to the outer and inner extents of the ellipse, respectively. We use these as inner and outer extents of the ellipse orbits with major axis sizes of $72 \text{ pc} < a < 146 \text{ pc}$. The ℓb and ℓv projections of the median, inner, and outer ellipse extents are shown in Figure 5. Colored markers represent NF positions, where bluer points indicate more near-sided positions (i.e. more positive d_{NF} values), and red is more far-sided values (negative d_{NF}).

4.3. Relative positions of clouds and comparison to best fitting x_2 orbits

The posterior PPDFs can be projected onto the best fitting orbital models to obtain LOS distances for all CMZ clouds. To explore the 3D distribution CMZ clouds, we use the median output ellipse parameters and inner/outer extents reported in Table 3 to create a top-down view of the CMZ. To project the NF positions to LOS distances for a given orbit, we use the nearest LOS point on the ellipse (R_{min}), and the furthest point (R_{max}) based on the outer ellipse extents to project the normalized -1 (far) to +1 (near) scale into a distance from the GC in parsecs using a simple formula:

$$y_{\text{pc}} = \frac{(y_{\text{NF}} + 1)}{2} \cdot (R_{\text{max}} - R_{\text{min}}) + R_{\text{min}} \quad (10)$$

Where y_{NF} is the top-down near (+1) vs far (-1) position on the same scaling as the PPDFs. For each cloud in the catalog, we then project the PPDF peak position (d_{NF}) onto the ellipse, which converts the normalized d_{NF} value into parsecs. Similarly, we convert the CI68 to physical units by multiplying this value by the LOS width of the ellipse ($\sigma \cdot (R_{\text{max}} - R_{\text{min}})$).

We report the LOS positions obtained from projecting each cloud in Table 1 onto the outer ellipse. The LOS uncertainties are calculated as the standard deviation of the positions from projecting onto each of the three ellipse extents (the standard deviation of y_{min} , y_{median} , y_{max}). The top-down projected positions and uncertainties for each cloud are shown in Figure 6. Blue and red colors indicate more-likely near or far-sided positions, respectively. Clouds which were included in the fitting are denoted by circular markers, with colors corresponding to the posterior PPDF peak, and sizes based on the effective radii obtained in *Paper III*. Black ‘x’ markers denote clouds which were not incorporated in the orbital fitting. Error bars correspond to the LOS uncertainties

of the projected positions. The conversion of PPDFs to distances introduces an approximately 32% systematic error to the LOS estimates, based on the spread of LOS values between the three ellipse extents. A 32% systematic error bar is shown in the upper left of Figure 6. We ask readers to regard the projected LOS distances qualitatively and refer to the relative positions of clouds as a more confident measure of positions from the fitting.

5. DISCUSSION

5.1. The 100 pc ring

The posterior PPDF results indicate the relative NF positions of CMZ clouds in the catalog on the normalized -1 to +1 scale. The nearest clouds include the contiguous dust ridge between the Brick and SgrB2 ($0.2 \lesssim \ell \lesssim 0.6$). The densest CMZ cloud, the Brick (ID 17b) has a normalized $d_{\text{NF}} \sim 0.69$, placing it confidently in front of the GC. ID 22 (clouds e&f) has the nearest value in the catalog of $d_{\text{NF}} \sim 0.84$, with a higher relative probability ($A \sim 40$) than the Brick’s peak value ($A \sim 13$), due to its very strong absorption, flux ratio, and correlation coefficient measurements.

In addition to the dust ridge clouds, there is a stream of near-sided structures between $-0.5 \lesssim \ell \lesssim -0.1$ and $b \lesssim -0.05$, colloquially coined “the wiggles” due to the area’s corrugated velocity pattern, potentially related to gravitational instabilities (Henshaw et al. 2020, 2016a). The wiggles region covers catalog IDs 1, 3, 5, and 7, all of which have likely near-side PPDF positions. However, they overlap with a far-sided part of the best fitting ellipse. When viewed top-down in Figure 6, these clouds appear near the edge of the orbit, possibly transitioning between the near and far sides. The orbital model from Kruijssen et al. (2015) also finds the NF distinction of the orbit in this area ambiguous, as their model’s streams 4 and 2 are indistinguishable in this region.

Only 10 masks in the catalog have far side distinctions, mostly located near the SgrA* region. The furthest cloud is ID 15, located at $(\ell, b) = (0.014, -0.016)$ with likely position $d_{\text{NF}} = -1.107$ which is heavily influenced by strong absorption measurements. Determining likely positions for objects in the Sgr A region, between $-0.1 \lesssim \ell \lesssim 0.15$, is particularly difficult since many of the NF methods, including the flux difference, flux ratio, and absorption measures are quite sensitive to uncertainties and variation in the bright background emission. The clouds in this region, as well as the Sailfish (ID 20) seem to align well with the far-side stream of the ellipse, with fairly high relative probabilities.

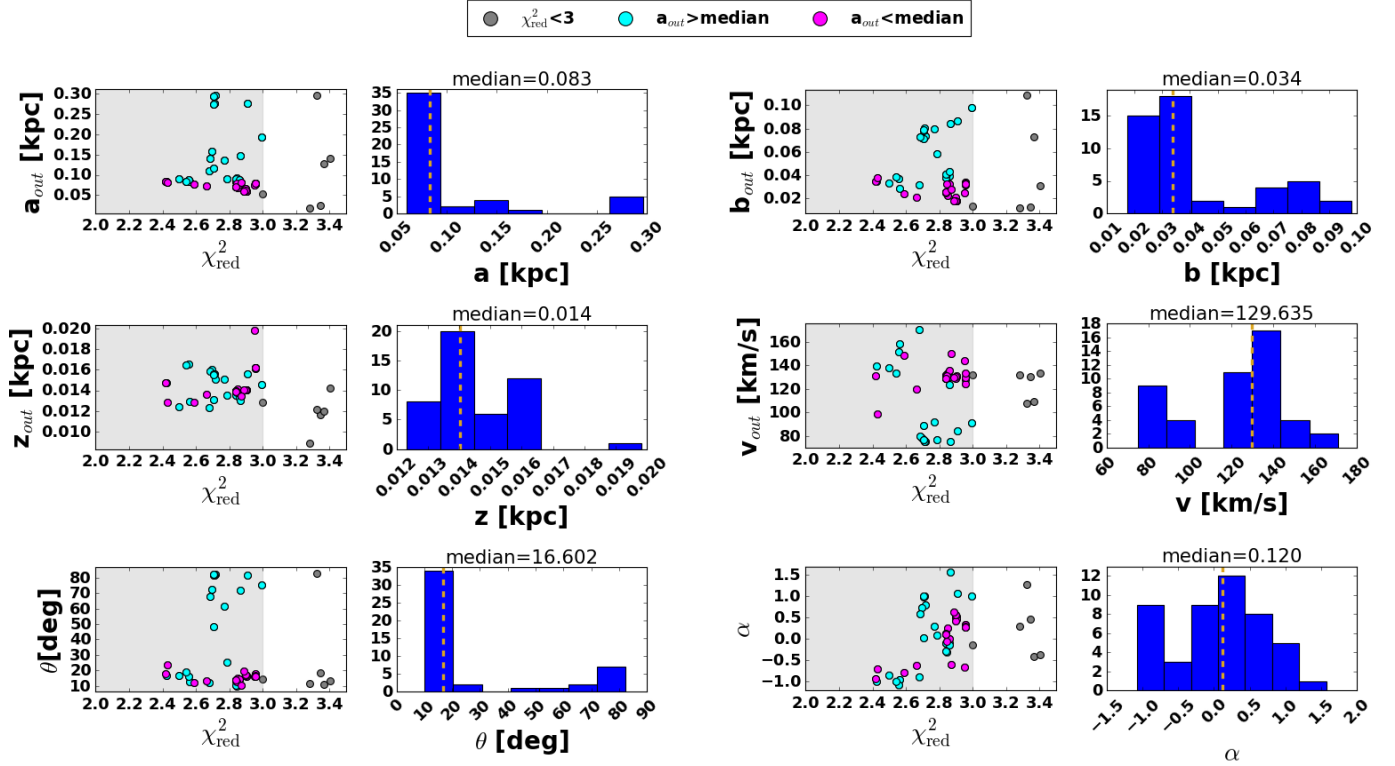


Figure 4. Left-hand panels show χ_{red}^2 values for output parameter values from the parameter grid search. The gray shaded region covers the χ_{red}^2 range $1 < \chi_{\text{red}}^2 < 3$ where the majority of outputs converge. Cyan (magenta) points correspond to outputs for ellipses with a major axis greater (less) than the median a_{out} value. Gray points note output values with $\chi_{\text{red}}^2 > 3$, indicating poor fits which are excluded from the histograms. Right-hand panels show histogram distributions of the output parameter values which lie within the gray shaded region from the left panel plots, along with the median output value (gold dotted line).

5.2. Comparisons with current LOS distance estimates to CMZ clouds

The LOS positions for a handful of clouds have been widely discussed in the literature. Using the top-down projection as described in Section 5.1, we compare their relative positions to the x_2 orbits and the GC.

The Brick: Our top-down projection places the Brick at a distance of 75 ± 26 pc on the near side of the CMZ. The position of the brick has been debated in the literature, with confident nearside placement based on its stark absorption features (Nogueras-Lara et al. 2021; Walker et al. 2025; Lipman et al. 2025), though some constraints place it on the nearest edge just outside of the CMZ (Zoccali et al. 2021). We find the Brick is not the most near-sided cloud, as the PPDF for Cloud e&f peaks at an even more near-sided position. Our results corroborate estimates placing the brick on the near side on the GC, but still within the CMZ.

20 and 50km s⁻¹ Clouds: The 20 (ID 9) and 50km s⁻¹ clouds (ID 10) were excluded from the orbital fitting, but their posterior PPDFs allow us to interpret their relative positions in the CMZ. Our top-down projection places them at 43 ± 19 pc and 31 ± 14 pc in front

of SgrA*, respectively. The clouds are also connected by a ridge of material (see Herrnstein & Ho 2005; Nogueras-Lara et al. 2026). Although their location is controversial, many models place the clouds quite close to SgrA* or curving slightly behind. The close proximity to SgrA* is typically justified by the non-illumination from X-rays (Chuard et al. 2018; Stel et al. 2025), evidence of interactions with the CND (e.g. Tsuboi et al. 2018), and interactions between the 50km s⁻¹ Cloud and the SgrA East supernova remnant (Genzel et al. 1990; Herrnstein & Ho 2005; Lee et al. 2008) which has been proposed to lie close to the CND and behind SgrA* (Yusef-Zadeh & Morris 1987; Pedlar et al. 1989).

However, dynamical models and absorption measurements strongly favor near-side interpretations for both clouds. Sofue et al. (2025) projects their distances onto inner spiral arms of the CMZ, placing the 20km s⁻¹ cloud 42 pc in front and the 50km s⁻¹ cloud between 7 – 42 pc in front, depending on its association with Arms III or V. Additionally, the Kruijssen et al. (2015) open stream orbital model places them ~ 50 pc in front of SgrA*. Mills et al. (accepted) justify the near-side placement by proposing an alternative interpretation of radio constraints, with Sgr A East being

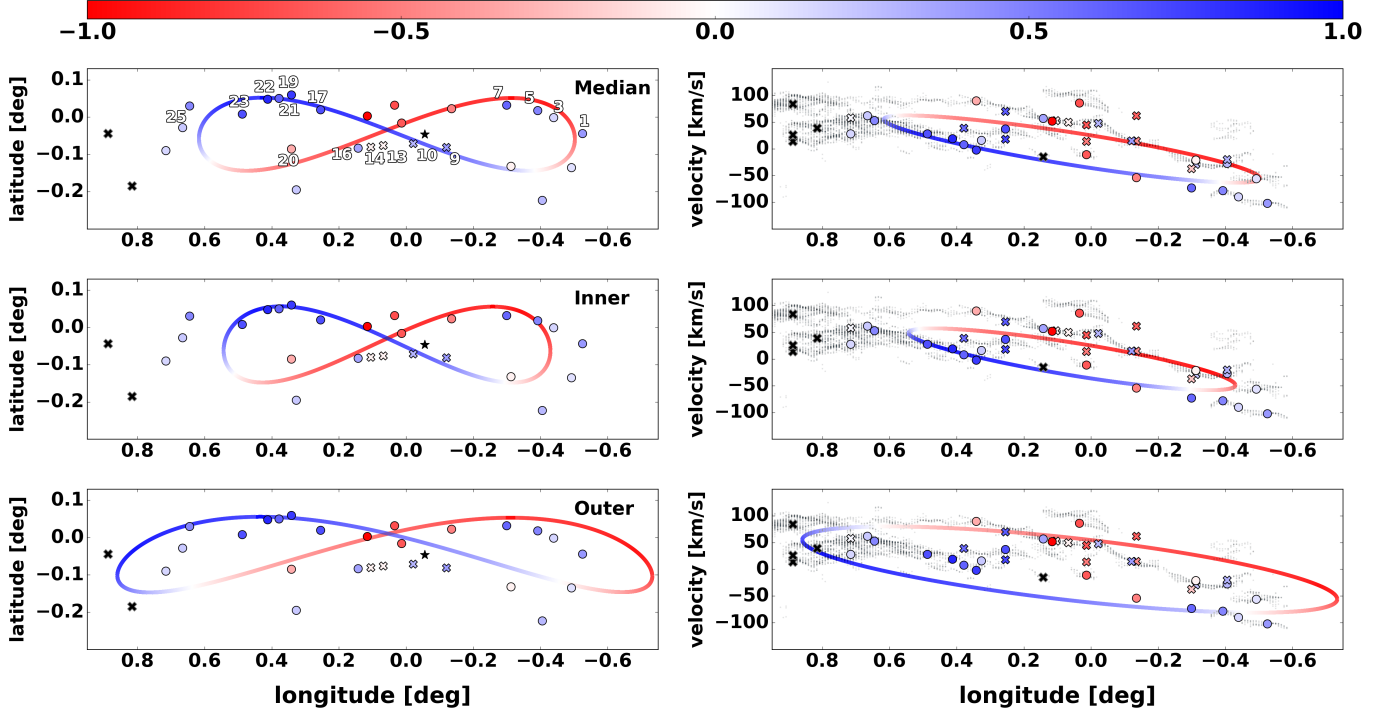


Figure 5. The parameter grid search results in a range of best fitting x_2 elliptical orbits for the star forming ring. This figure shows (ℓ, b) (left) and (ℓ, v) (right) projections of the best fitting parameters summarized in the right-hand section of Table 3. Blue colors indicate more-likely near-sided positions, while red indicates more likely far-sided. The black star indicates the location of SgrA*. Marker colors correspond to their most likely posterior PPDF positions. Colored x markers indicate clouds that have NF distinctions based on their PPDFs, but are not included in the fitting procedure. Black x markers are clouds which are not included in the fitting procedure, and for which a formal NF distinction is not shown, due to the limited data and association with the majority of CMZ data points. Gray background points correspond to the spectral decomposition of MOPRA HNC data from Henshaw et al. (2016b). ID numbers for well-known clouds are noted in the top left panel.

seen in absorption in front the GC synchrotron background, placing it in front of Sgr A West. Our results agree with these near-side interpretations, and support the interpretation that the clouds could be actively infalling off of an inner x_2 orbit towards the CND, making them kinematically distinct from the main elliptical structure.

The Three Little Pigs: The Stone (ID 13) and Sticks (ID 14) clouds are within 15 pc of SgrA* in the (ℓ, b) projection, while the Straw cloud (ID 16) lies at about 40 pc. X-ray observations confidently constrain the LOS positions between 30 pc behind to 20 pc (10 pc) in front of the GC for the stone (sticks) cloud (e.g Clavel et al. 2013; Chuard et al. 2018; Stel et al. 2025). The clouds are unlikely to be more than 20 pc in front of the GC, as they would not have been observed as illuminated by a flaring event otherwise. Our results place both clouds within ~ 10 pc behind SgrA*.

The estimated distances imply the clouds do not lie on an x_2 orbit, but are instead part of an inner spatial region which may be kinematically distinct from the star forming ring. Our projected model places the Straw cloud even further in front, meaning it may eventually

be illuminated by the same X-ray event as the stone and sticks clouds in the future.

Sgr B2 and Sgr C: The X-ray data for SgrB2 (ID 25) is well-documented and suggests a lower limit for the LOS distance of ~ 50 pc in front of the GC (Chuard et al. 2018; Stel et al. 2025), with various systematic uncertainties. Our results place the cloud at 23 ± 15 pc in front of the GC. However, the systematic uncertainty of this estimate is quite high, due to the cloud being on the edge of the orbit where there is less deviation in its projected distance between the ellipses. We also note high uncertainties in this area due to the complexity of the Sgr B2 region and variable ISM conditions. X-ray constraints for Sgr C (ID 2) place strict lower limits for parts of the region of at least ~ 30 pc in front of the GC (Chuard et al. 2018; Stel et al. 2025) with some estimates placing it on a nearer edge of the CMZ around $\sim 70 - 100$ pc (Ryu et al. 2013). Our projected model places Sgr C at 14 ± 18 pc on the near side, which is within range of uncertainties for lower X-ray limits. Sgr C also appears to lie at the edge of our best fitting orbital model, potentially wrapping around near to far

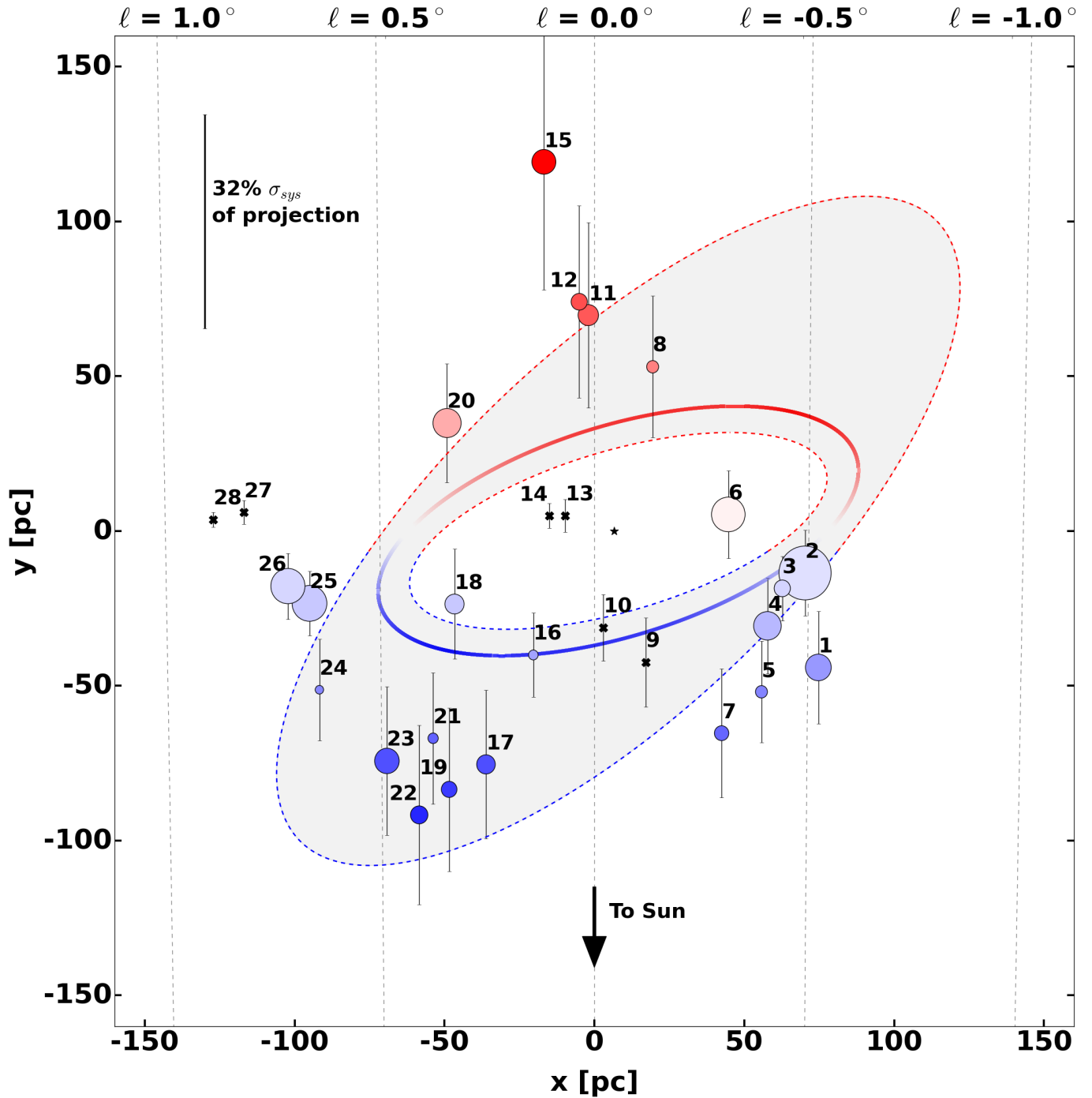


Figure 6. We present a preliminary top-down view of the best fitting CMZ orbits, as well as projected positions of all cataloged molecular clouds based on the outer ellipse model from the parameter grid search. The above figure shows a top-down projection of the orbits summarized in Table 3. The middle ellipse corresponds median x_2 orbit from the parameter grid search. The gray shaded region is bound by the best-fit inner and outer extents, and indicates a range of possible x_2 orbits. Blue and red colors indicate more-likely near or far side positions, respectively. Positions of CMZ clouds which were included in the x_2 fitting are denoted by circular markers, with colors corresponding to the location of the Gaussian peak in the posterior PPDF for each cloud, and sizes corresponding to the effective radius of each cloud as reported in Walker et al. (2025). Black ‘x’ markers denote clouds which were not incorporated in the x_2 fitting. Error bars correspond to the uncertainties of the projected positions calculated using the PPDF CI68 values and standard deviation in the projected distances on all three ellipses for each cloud. A 32% systematic error bar for the LOS distance projections is shown in the top left. The black star denotes the location of SgrA*.

sides of the outer orbital extent.

Overall, our results agree with current literature constraints, within our reported errors. The agreement supports our method’s ability to utilize LOS distance constraints in combination with NF placements, and produce LOS distance estimates that are reasonably in line with preliminary results from various datasets.

5.3. CMZ size and morphology

5.3.1. Is the CMZ a simple ring?

While it is known that the size of the CMZ is controlled by the Galaxy’s gravitational potential and the Galactic bar (e.g. Sormani et al. 2015), the exact size and shape is still debated. Most outputs from the parameter search result in major axes between $60 < R < 296$ pc, with our reported inner and outer extents between $\sim 72 < R < 146$ pc. This implies a thickness of about two times the inner radial extent, and appears visually comparable to extragalactic CMZs with thick nuclear ring such as NGC 1300 or NGC 1433.

Observational studies of the CMZ report various estimates for the outer extents. Many studies tend to focus on the 100 pc stream. However, there is evidence to support that both the contentious 1.3° complex as well as seemingly bright, contiguous material out to 1.5° should be considered part of the CMZ (see Battersby et al. 2025a; Gramze et al. 2023). Theoretical estimates of CMZ sizes are also quite variable, with the largest possible x_2 orbits lying anywhere from $R = 200$ pc to $R = 1$ kpc (Athanasoula 1992; Sormani et al. 2015). Additionally, while the idealized x_2 orbits are exactly perpendicular to the Galactic bar, the observed orientation of the bar’s major axis and the Sun-GC line is approximately $20 < \theta < 30^\circ$. Our median orbit falls in the observed range within a 1σ uncertainty. Many effects can change the orientation of x_2 orbits, such as gas self-gravity which produces angles similar to those seen in simulations from Tress et al. (2020). The x_2 ellipse fitting returns reasonable sizes and a variety of orbits for gas on the main star forming ring, rather than a single best fit. We do not explicitly test for a consistent family of orbits in this study. However, the various extents from the parameter search could also be interpreted as corresponding to families of x_2 orbits.

We also compare the NF positions of our cataloged clouds in PPV space against four different 3D orbital geometries in Figure 7. The models include our median fitted ellipse (top left); spiral arms or spirals similar to those proposed by Sofue (1995, 2022); Sofue et al. (2025) (see also Sawada et al. 2004; Ridley et al. 2017) (Sofue; top right); open streams based off of an open x_2

orbit from Kruijssen et al. (2015) (KDL; bottom left); and a closed elliptical x_2 orbit which assumes a constant orbital velocity, proposed by Molinari et al. (2011) (Molinari; bottom right). Note the projection used for the Sofue model is an approximation based on the KDL streams (see Henshaw et al. 2016b).

The morphology of the CMZ is complex and unlikely to lie perfectly on a closed ellipse (Kruijssen et al. 2015; Tress et al. 2020). Some of these orbits may be populated by gas, while others may be cleared out due to variations in the environment. However, a family of elliptical x_2 orbits, similar to those presented in Binney et al. (1991), can fit the average observed gas distribution quite well, as seen by the KDL and our closed ellipse models. These geometries have similar distance and kinematic interpretations for the dust ridge and wiggles region, but all struggle to consistently explain the motion of material further inside the ring that could be infalling towards the CND and SgrA*. Alternatively, the Sofue spiral arms model allows for separate streams to address conflicting kinematics. MHD simulations of the CMZ seem to show clear features for both average x_2 elliptical orbits and inspiralling features towards the center (e.g. Tress et al. 2024), meaning that modeling the inner region as a spiral extending off of the x_2 orbit could result in a reasonable geometry.

Both our model fittings and the 3D geometries in the literature seem to suggest that the 3D structure of the CMZ is kinematically and spatially complex, and cannot be simplified to a single contiguous orbital stream.

5.3.2. Asymmetries along the line-of-sight

Previous studies of the CMZ have noted that gas is preferentially distributed at positive longitudes (Bally et al. 2010; Longmore et al. 2013; Battersby et al. 2025a; Walker et al. 2025). Our results highlight another asymmetry: most of the clouds in the catalog seem to be placed on the near side of the GC, which is consistent with other elliptical models (Kruijssen et al. 2015; Walker et al. 2025). The near-side features include the dust ridge, coinciding with the dense areas of the CMZ with more active star formation compared to the negative longitudes. However, we also see that most of the clouds in the western region, which are not as prolifically star forming, are also on the near side, though relatively further back than the dust ridge. The far-side clouds are those in the Sgr A region, an area with high systematic uncertainties due to proximity to SgrA*.

Although our analysis places the majority of CMZ clouds on the near side, we argue this is not the result of observational bias. Both Herschel column density maps (Battersby et al. 2025a) and molecular gas

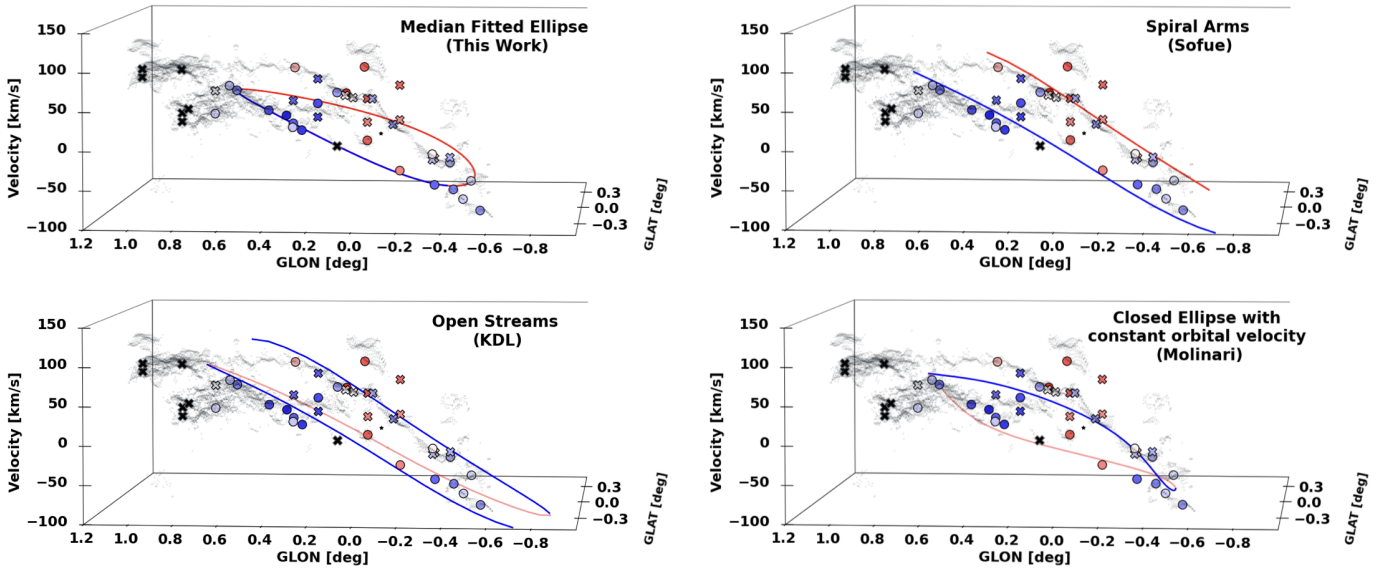


Figure 7. We present the NF positions of our cataloged clouds against four different 3D orbital models in PPV space plotted over spectral decomposition of MOPRA HNC0 data from Henshaw et al. (2016b) (gray background points). The models include the median fitted ellipse from this work (top left); two spiral arms similar to those proposed by Sofue (1995) (top right); open streams based off of an open x_2 orbit from Kruijssen et al. (2015) (bottom left); and a closed x_2 orbit which assumes a constant orbital velocity, proposed by Molinari et al. (2011) (bottom right). Markers are the same as presented in Figure 5. Blue and red colors indicate likely near or far positions, respectively. The black star denotes the position of SgrA*.

(Jones et al. 2012; Ginsburg et al. 2015, 2016) show more diffuse emission which is coincident with the far side of our model. Despite the systematic uncertainties, it is reasonable to assume that our detection of structures is not biased or incomplete at these wavelengths. Additionally, the individual NF metrics independently report NF asymmetries, as highlighted in *Paper III* and *Paper IV*. Both analyses find most clouds on the main CMZ orbit lie on the near side, with only a handful of clouds having confident far-side distinctions. The star count ratio finds a similar distribution as the $8\mu\text{m}$ methods. Extragalactic CMZs also show asymmetric gas distributions, such as the central rings of NGC 3351 (Sun et al. 2024), NGC 1300 and NGC 1672 (Gleis et al. 2026) which show closed rings with asymmetric CO emission; or M83 for which about two-thirds of gas lies on one side of the orbit (Callanan et al. 2021). While systematic uncertainties could present biases for individual NF methods, the overall LOS asymmetries are likely real and not necessarily unexpected.

Strong LOS asymmetries are supported by theory, as gas on x_2 orbits is unlikely to be uniformly distributed. From a computational standpoint, MHD simulations show that the CMZ may go through epochs where gas is skewed to one side (Tress et al. 2020, 2024), meaning large anisotropies may point towards collisions or merging of material from the bar lanes disrupting large amounts of gas off of the average orbit.

The non-uniform distribution of gas in the CMZ is also seen in velocity space. In particular, the spectral decomposition of MOPRA HNC0 data from Henshaw et al. (2016b) shows distinct streams which match our best-fit model extents reasonably well, as shown in the PPV diagram of Figure 8. We also note a closed loop connecting gas between longitudes of $0.1^\circ < \ell < 1^\circ$ which stretches between the ellipses. We refer to this structure as the ‘ lv loop’, highlighted as golden points in Figure 8. The physical interpretation and origin of this loop are unclear. Similar features have been seen in simulations such as Tress et al. (2020, 2024) where gas is sheared from collisions with the dust lanes, causing large disruptions in the orbital motions of bulk gas. The lv loop could also be indicative of gas falling onto inner x_2 orbits or stretching between local minima. These features make fitting a precise ellipse to the data difficult, as the gas becomes spread out between multiple orbits.

6. UNCERTAINTIES

6.1. Uncertainties and Limitations of the PPDF method

The Bayesian framework presented in Section 3.1 flexibly combines datasets with position or distance-based constraints for NF estimates in the CMZ. While the framework’s main advantages are its flexible parameters and weighting scheme, the creation of prior distributions is largely based on user interpretation, which requires justifications and consideration of systematic bias.

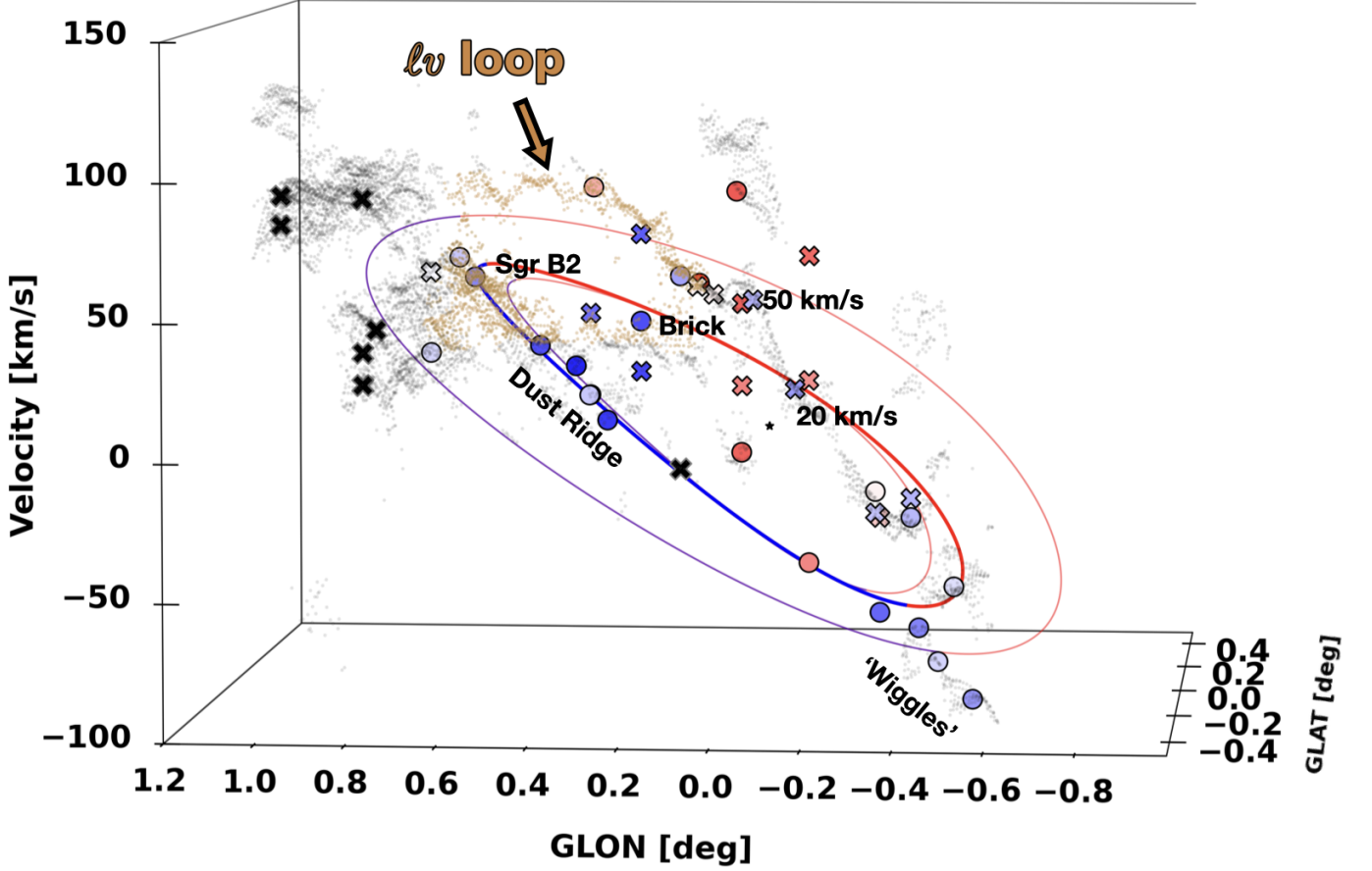


Figure 8. The output of the orbital modeling is determined by fitting the clouds in PPV space, as well as their NF posteriors from the PPDFs. This figure shows the best fitting orbits and clouds on top of the spectral decomposition of MOPRA HNC data from Henshaw et al. (2016b) (gray background points). The median ellipse is shown as a thicker line compared to the inner and outer extents. We highlight a closed loop of gas, colored with gold points, referred to here as the ‘*lv* loop’, which may be indicative of shearing or disruption events causing gas to deviate from the orbital streams. Markers are the same as presented in Figure 5. Blue and red colors indicate likely near or far positions, respectively. The black star denotes the position of SgrA*.

The quality of PPDF results are dependent on the precision of the input data. More constrained data will have a stronger impact on the posterior fits, as evidence by the confident absorption data which dominate the posterior fittings. While the higher weighting of this method also affects the resulting combinations, the spread and amplitude of the priors have much larger impacts. The most uncertain results are typically in areas where data is omitted due to systematic uncertainties (e.g. the Sgr A region) or is unavailable (e.g. no absorption estimates for IDs 27 – 31). Some methods may systematically place clouds on either the near or far side, and the lack of confident metrics in these areas could lead to systematic NF preferences. The inclusion of more data across the entire catalog, especially LOS distance estimates from NIR dust extinction methods, proper motions, or parallax measurements, would greatly constrain the PPDF posteriors and mitigate the systematics from less certain methods.

The second limitation of the PPDF method is the normalization procedure. All data are normalized to the (-1,1) scaling before the posterior combination, which estimates positional constraints well for the majority of clouds. However, at present, there does not exist a clear method to compare LOS distances with NF positions of cloud for which distance estimates are unavailable. Physical distance priors must be projected onto the (-1,1) scaling, which requires a prior assumed CMZ radius. In this case, we use the typical assumption from the literature of a 150 pc CMZ radius. Using different initial radii will impact the LOS metrics, as larger (smaller) initial guesses will place clouds further from (closer to) the center. The effects of an initial guess must therefore be well-justified if using LOS distances as priors. Future iterations of the method may be improved by incorporating future distance constraints for a large sample of CMZ clouds, making it possible develop LOS likelihood functions for the PPDFs.

6.2. Uncertainties of the ellipse fitting method

The x_2 ellipse fitting generally produces reasonable fits to the observed data, and does not converge on a single orbit. Overall, the fitting procedure is quite sensitive to both the initial parameters and the PPDF priors. For example, incorporating 50-100% systematic errors for all methods results in the posterior PPDFs being pulled closer 0 with large uncertainties. Those broad PPDFs can greatly impact the parameter grid outputs, resulting in incredibly compact CMZs ($20 < R < 80$ pc). While the PPDFs are good indicators for relative positions of clouds, we present the fitting procedure as an exploratory method to compile multiwavelength measures of CMZ cloud positions. The reported CMZ model extents are best used as starting points for future improvements.

The spread in the reported CMZ extents could be affected by the minimization method. In this study, we use the Nelder-Mead minimization method which performs with higher accuracy and broader sampling of parameter space compared to the typical least-squares method. However, the Nelder-Mead simplex can be quite sensitive to initial guesses, and can lead to any parameter falling into local minima regardless of the input.

The inclusion new of structures could also impact the fitting, and potentially result in different ellipse sizes. For example, Cloud IDs 27 – 31 were not included in the fitting procedure due to the lack of a variety of NF metrics (the clouds only have results from dust extinction and star count metrics, but no available absorption data) and their separation from the majority of clouds near SgrA*. Including these points could impact the size and orientation of the ellipse. Inclusion of foreground structures could also impact the extents and orientation of the ellipse, particularly if their PPDFs are tightly constrained. For example, it is possible IDs 4a and 4b could be foreground structures based on their latitude positions. However, their PPDFs are quite consistent with the surrounding clouds in that region, so their individual impact on the fitting is not high. A more impactful limitation of the current method is the simplification of each cloud to a single point for the orbital fitting, which neglects extended features. Future work is planned to modify the fitting procedure for a pixel-by-pixel approach, and incorporate extended filamentary features (e.g. , Battersby et al. *subm*) to help constrain the extents of the gas streams.

We also note large systematic uncertainties associated with the top-down projection presented in Figure 6. While we confidently constrain the relative NF positions of clouds, there are many ways one could project the PPDFs onto the orbital model to obtain LOS distances.

The distance estimates shown in the figure and reported in Table 1 are based on projection of the PPDF positions on to the outer-most fitted ellipse extent. Thus, the distance estimates are dependent on the inner and outer extents, which set the possible LOS extents for the dataset. While the relative NF positions are robust for relative comparison of cloud locations, the distance estimates and LOS uncertainties are projection-dependent.

7. CONCLUSIONS AND SUMMARY

We introduce a flexible Bayesian framework to combine different datasets of various near versus far position and line of sight distance estimates for CMZ clouds onto a single quantitative scale. We use estimates from dust extinction, molecular line absorption, star count ratios, X-ray echoes, and stellar kinematics to find the posterior Position Probability Density Functions (PPDFs) for each structure in the CMZ cloud catalog presented in this paper series. We then create an optimized fitting procedure with the `lmfit` python library to find a best fitting x_2 orbit for CMZ clouds by minimizing the residuals between the orbit and posterior PPDFs.

The PPDF and x_2 fitting methods are intended to be continually updated and modified with new data. The relevant code for this paper series are publicly available via: <https://centralmolecularzone.github.io/3D-CMZ/>. The maps and data products can be found on Harvard Dataverse: <https://dataverse.harvard.edu/dataverse/3D-CMZ>

Our main findings from the combined PPDF and orbital fitting methods include the following:

- By exploring a range of input major axes between 10–300 pc, we find that the fitting procedure converges on a population of ellipses spanning major axis radii of $60 < a < 296$ pc. We find an inner and outer average semi-major extents of the CMZ to be 72 pc and 146 pc, and a median extent of 83 pc. These results support the interpretation that gas orbits in the CMZ are more complex than a single 100 pc ellipse.
- The median best fitting orbit and estimated LOS distances are consistent with other elliptical orbital models (e.g. [Kruijssen et al. 2015](#); [Molinari et al. 2011](#)). However, elliptical models struggle to kinematically explain material which may lie closer to SgrA* along the LOS. Many CMZ clouds may exist on a family of x_2 orbital ellipses between the inner and outer extents identified in the fitting procedure. An x_2 orbital model may require additional complexity inside of the average orbit, such as an inspiralling component, to explain infall.

- We present a top-down view of our CMZ model and estimate LOS positions to clouds by projecting the PPDF peak positions onto the outer ellipse extents.
- Our projected LOS distances agree with many current distance constraints from the literature. In particular, our results support evidence that the three pigs may lie much closer to SgrA*, within 10 pc. Additionally, our results place the 50 and 20km s⁻¹ clouds at 31 ± 14 pc and 42 ± 19 pc in front of SgrA*, which disagrees with models placing the clouds near the CND or behind SgrA*. These structures may be actively falling inwards from an inner x₂ orbit, making them kinematically separate from the average gas flows.
- We highlight prominent asymmetries along the line of sight, with most clouds located on the near side of the CMZ. An overall near-side preference for the gas is found independently in all NF methods, and mirrors similar distributions seen in extragalactic CMZs (e.g. Callanan et al. 2021; Gleis et al. 2026; Sun et al. 2024) and MHD simulations (e.g. Tress et al. 2020) when large parcels of gas from the bar lanes collide with orbiting material.
- We note the existence of an *ℓv* loop feature seen in molecular data from MOPRA, which may be the result of shearing events disrupting gas on x₂ orbits, and possibly inducing infall between orbits.

Our analysis highlights the complexity of the CMZ gas distributions, which may not be simply fit by a single elliptical orbit. We note the need for further study of the family of possible orbits, and suggest that combining both elliptical x₂ and spiral features may provide a reasonable geometry to explain both average CMZ mass flows and infalling material. More detailed analysis of individual clouds, including LOS distances will help strengthen the modeling, and could help determine which structures belong to various orbits.

ACKNOWLEDGMENTS

D. Lipman and C. Battersby gratefully acknowledge funding from the National Science Foundation under Award Nos. 1816715, 2108938, 2206510, and CAREER 2145689. D. Lipman also acknowledges funding from the NASA Connecticut Space Grant Consortium under PTE Federal Award No: 80NSSC20M0129. C. Battersby also acknowledges funding from National Aeronautics and Space Administration through the Astrophysics Data Analysis Program under Award “3-D MC: Mapping Circumnuclear Molecular Clouds from X-ray to Radio,” Grant No. 80NSSC22K1125.

D. Walker acknowledges support from the UK ALMA Regional Centre (ARC) Node, which is supported by the Science and Technology Facilities Council [grant numbers ST/Y004108/1 and ST/T001488/1].

F. Nogueras-Lara gratefully acknowledges financial support from grant PID2024-162148NA-I00, funded by MCIN/AEI/10.13039/501100011033 and the European Regional Development Fund (ERDF) “A way of making Europe”, from the Ramón y Cajal programme (RYC2023-044924-I) funded by MCIN/AEI/10.13039/501100011033 and FSE+, and from the Severo Ochoa grant CEX2021-001131-S, funded by MCIN/AEI/10.13039/501100011033.

R. Klessen acknowledges financial support from the ERC via Synergy Grant “ECOGAL” (project ID 855130), from the German Excellence Strategy via the Heidelberg Cluster “STRUCTURES” (EXC 2181 - 390900948), from the German Science Foundation under grant KL 1358/22-1, and from the German Ministry for Economic Affairs and Climate Action in project “MAINN” (funding ID 50002206).

A. Ginsburg acknowledges support from the NSF via AAG 2206511 and CAREER 2142300.

M. Clavel acknowledges financial support from the Centre National d’Etudes Spatiales (CNES).

M. C. Sormani acknowledges financial support from the European Research Council under the ERC Starting Grant “GalFlow” (grant 101116226) and from Fondazione Cariplo under the grant ERC attrattività n. 2023-3014.

This work made use of Astropy:¹ a community-developed core Python package and an ecosystem of tools and resources for astronomy (Astropy Collaboration et al. 2013, 2018, 2022).

APPENDIX

¹ <http://www.astropy.org>

A. JUSTIFICATION FOR MODELING PPDF PRIORS AS GAUSSIAN

The Bayesian synthesis of observational data presented in Section 3.1 is a flexible framework that allows the user to assume a distribution shape of their choice for any given prior. For this study, we chose to model most of the prior distributions as Gaussian, given the methods report a single median value for a cloud, rather than a continuous distribution.

We explored different uncertainty estimations for the flux difference, flux ratio, star count ratio, and absorption methods, summarized in Figure A.1. For each method, we normalize a given cloud map using Eqn 2, and show the normalized counts (gray histogram) along with the median of the distribution (blue dash-dotted line) corresponding to the NF position for the prior (μ). The normalized prior used for the Bayesian synthesis is shown by the solid orange line. Most distributions are approximately Gaussian or log-normal. Each method has undetermined systematic uncertainties, so we focus less on perfectly representing the shape of the normalized maps, and more on creating a prior which represents the spread of the data overall. For the $8\mu\text{m}$ flux methods and star count ratio, we show unnormalized Gaussian distributions created using the median of the normalized map, and uncertainties determined by the standard deviation (pink dotted) or σ_{MAD} (purple). For these methods, the σ_{MAD} provides a better overall fit to the spread in the data, and is thus used for building the priors.

Paper III reported the absorption fraction value over the entire cloud masks. Here, we create absorption fraction maps to obtain statistical uncertainty estimates. The pixel-wise absorption fraction maps are created via: (GBT C-Band Continuum map + a cosmic microwave background estimate) / abs(H_2CO Min Intensity over the masked cube). The uncertainty estimate for the absorption method was originally set at 3σ based on the standard deviation of the un-normalized dataset. However, upon review, we investigated the error propagation of the normalized maps, as presented in Section 3.1. We show the un-normalized distributions with uncertainties from the error propagation (green dotted line) and $3\times$ the error (red dotted). The 1σ estimation almost exactly matches the standard deviation of the maps. We choose to model the absorption fraction Gaussian priors with the 1σ uncertainty from the error propagation, for the most robust estimation of the statistical errors.

The $70\mu\text{m}$ correlation coefficient is a single value summarizing the overall statistical correlation of the calculated cloud extinction and observed emission maps and is best reflected as a Gaussian with large uncertainties. As discussed in *Paper IV*, the method could be improved with more confident $70\mu\text{m}$ emission models to generate a unique, continuous NF position probability distribution. However, building such a distribution requires carefully constructed radiative transfer models for $70\mu\text{m}$ emission, which is outside the scope of this series of papers.

B. PPDF POSTERIOR PLOTS

The PPDFs for all CMZ clouds are presented in Figure B.1 below. The methods used to infer NF positions of individual clouds in the CMZ can be combined in a Bayesian framework to create a posterior distribution of NF likely positions for a given cloud on a normalized scale of -1 (far) to +1 (near). Here we show example prior and posterior PPDFs for six clouds in the catalog. The flux difference (orange dashed line) is used as a likelihood function, and is multiplied by distributions for the flux ratio (green), correlation coefficient (blue), absorption fraction (red), and star count ratios (yellow).

IDs 13 and 14 have prior data from X-rays (pink), and IDs 9 and 10 have prior data from stellar densities (brown). ID 16 is an empty submask, and thus has no prior or posterior information plotted.

After taking the product of the priors, we report the location of the peak (μ , vertical gray dash-dotted line), the relative probability peak (A), and the 68% confidence interval (CI_{68} , horizontal solid gray line), which are used to obtain a Positional PDF posterior distribution (PPDF; black solid line). The peak of the PPDF indicates the most likely NF position of the cloud. All distributions are normalized to unit integral probability.

C. DATA TABLE FOR BUILDING PPDF PRIORS

All information needed to build the prior PPDFs for near/far distinction methods is reported in Table 4. We provide this information for any method which distinguishes NF positions for clouds: the flux difference, flux ratio, correlation coefficient, absorption fraction, and star count method. These priors are all created by normalizing the values in the table using Equations 2, and constructing normalized Gaussian profiles, as discussed in Section 3.1. The priors from distance X-ray and stellar kinematic distance estimates are built in a different way, involving projection onto an assumed initial guess for an orbital model to normalized them to the same scaling as the NF distinction datasets. This is only done for five clouds, and refer the reader to Section 3.1 for details of how to construct these priors.

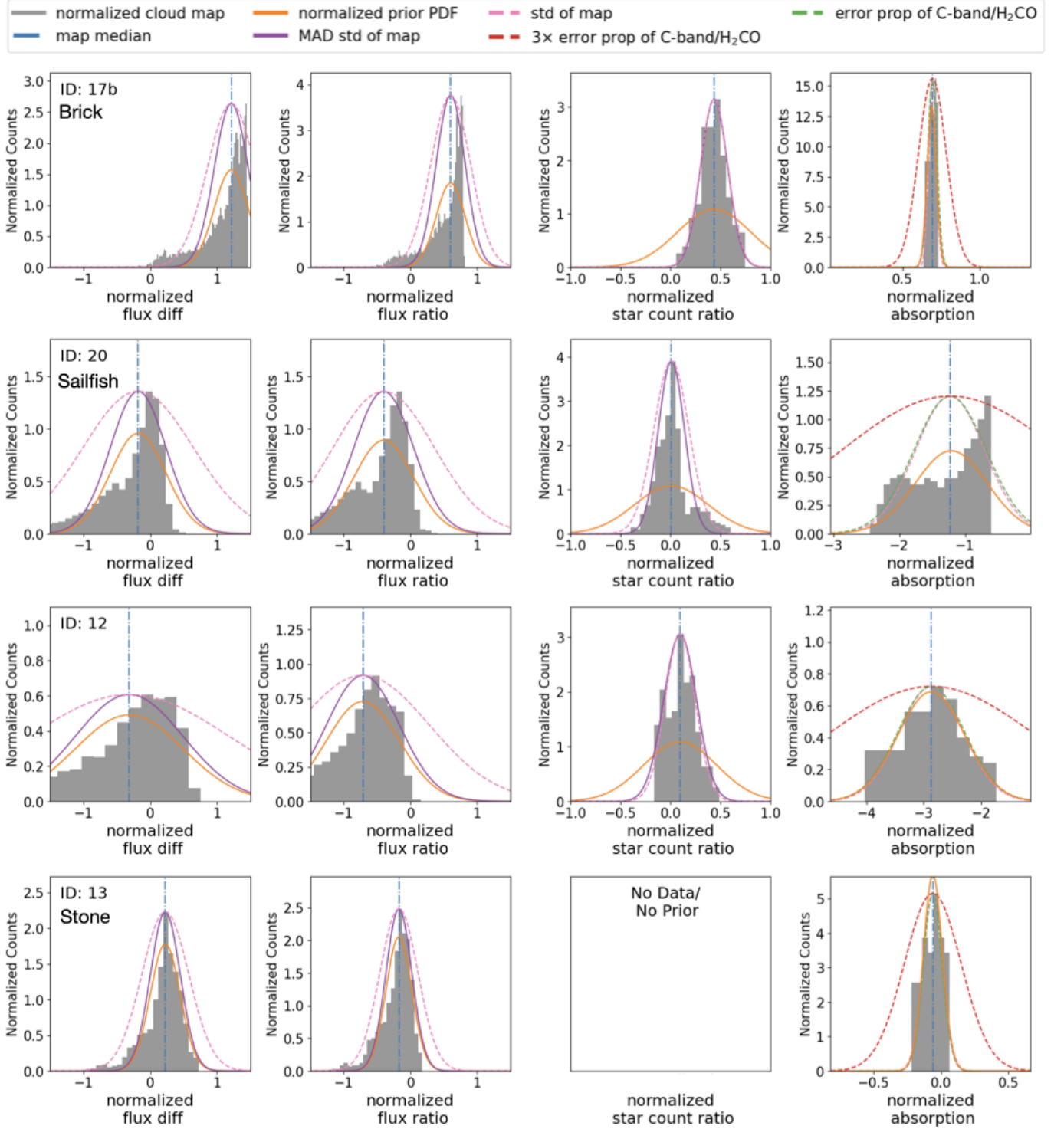


Figure A.1. Most normalized NF distributions can be approximated by a single Gaussian. We highlight four examples of clouds showing the distribution of normalized counts for the flux difference (first column), flux ratio (second column), star count ratio (third column), and absorption methods (fourth column). Each plot shows a histogram of the cloud maps with NF values normalized using Eqn 2 (gray), the median of the normalized map (blue dash-dotted line), and the normalized PPDF prior ultimately used for each method (orange line).

The first five columns of Table 4 are taken from Table 1 of Walker et al. (2025), including the leaf IDs of the cataloged clouds, the associated cloud names, central coordinates in degrees (l, b), and central velocity from HNC0

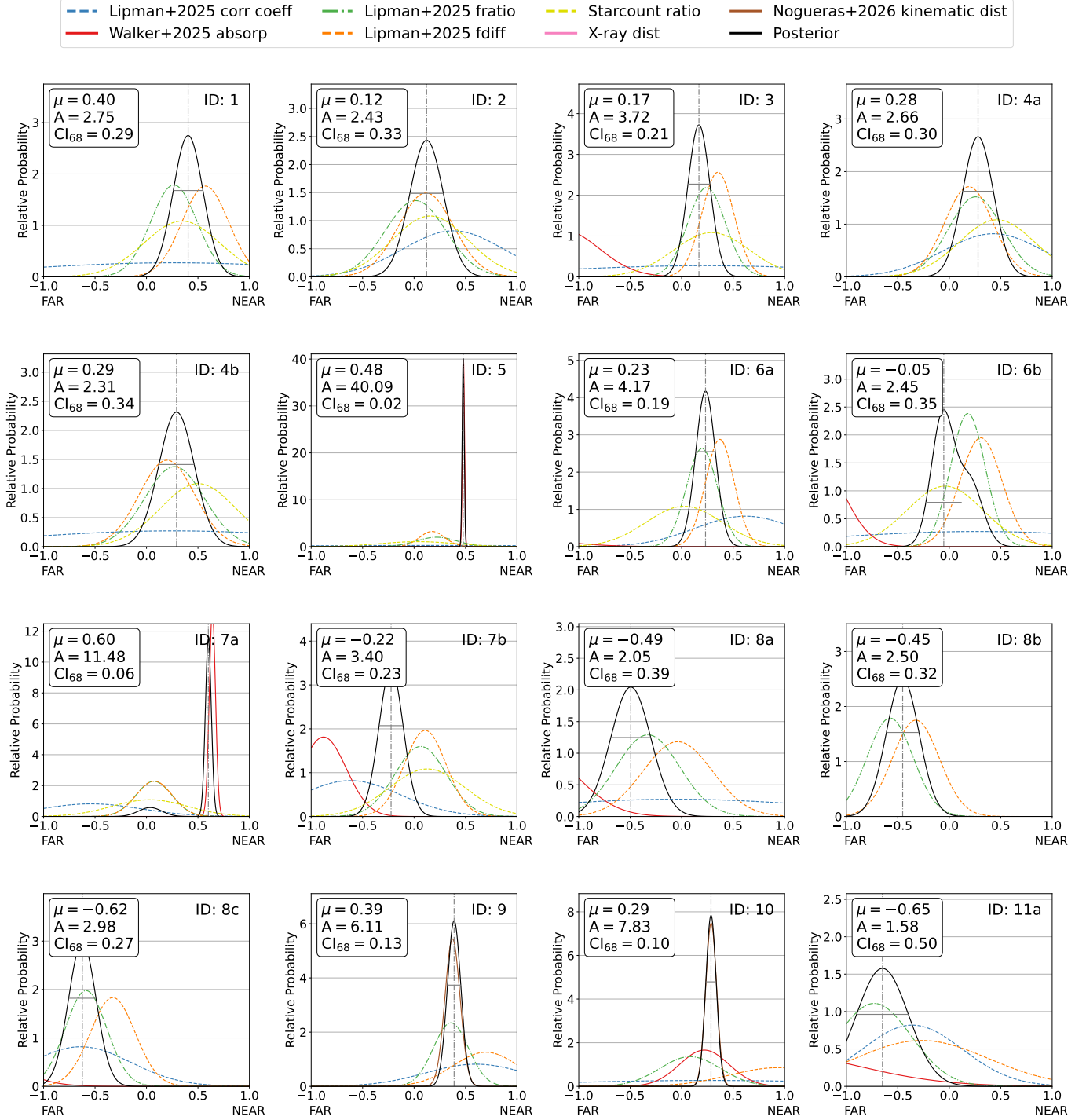


Figure B.1. Prior and posterior PPDFs for all cloud masks in the catalog. Each panel shows priors for different methods as colored lines, and the posterior is indicated by a black solid line. We report the location of the peak (μ , vertical gray dash-dotted line), the relative probability peak (A), and the 68% confidence interval (CI_{68} , horizontal solid gray line), which are used to obtain a posterior PPDF distribution used for the orbital fitting procedure in Section 3.2.

(v). The data metrics available to construct the PPDF priors for NF methods include: the median flux difference value, flux difference standard deviation, median flux ratio, flux ratio standard deviation, correlation coefficient, absorption

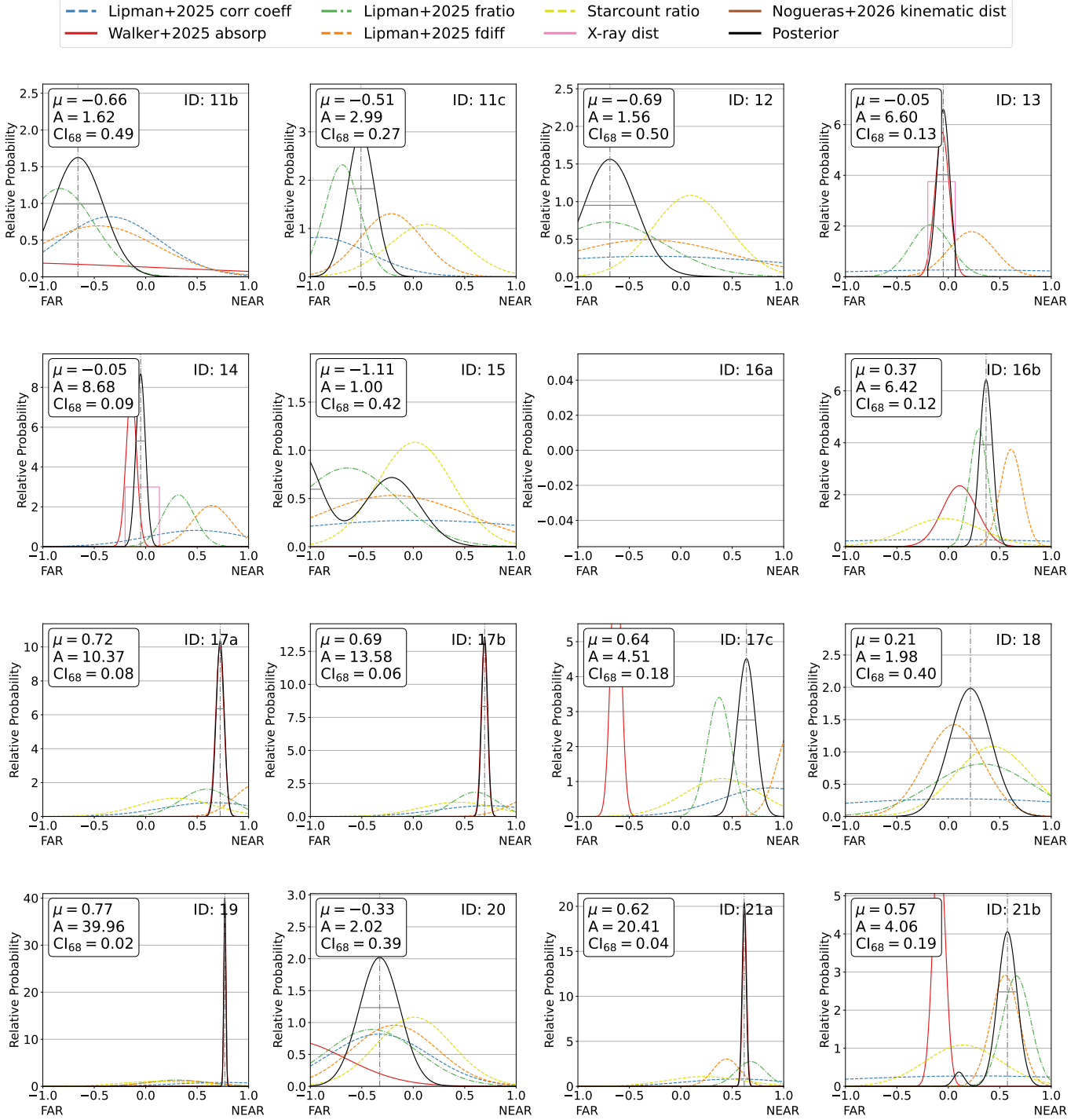


Figure B.1. (cont.)

fraction, absorption fraction sigma value, star count ratio, and star count ratio standard deviation. If a given method was not available or reported for a given cloud, we report the value as a “nan” in the table column. Otherwise, all numerical values for NF metrics are the reported values used to construct the NF method’s prior for that cloud.

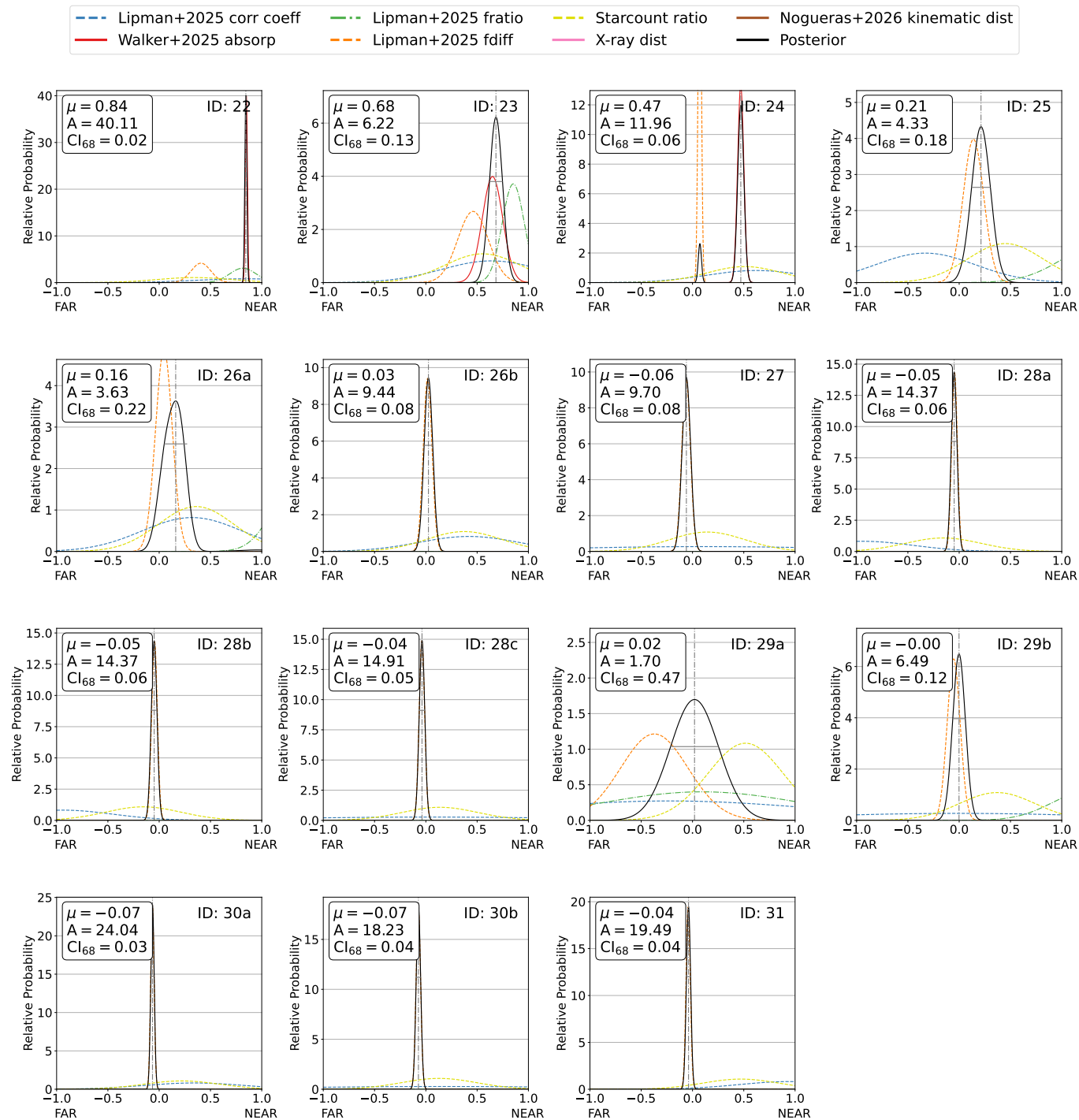


Figure B.1. (cont.)

Table 4. Information needed to build the prior PPDFs from the near/far distinction methods.

leaf id	cloud name	l	b	v	flux diff	flux diff	flux ratio	flux ratio	corr coeff	absorption	absorption	fraction σ	star count	star count	ratio	ratio stdv
		deg	deg	km/s	MJy/sr	MJy/sr	stdv	stdv	stdv	fraction	fraction	fraction σ	ratio	ratio	ratio	ratio stdv
1	G359.475-0.044	-0.525	-0.044	-102.0	-20.97	33.92	0.37	0.112	0.26	nan	nan	nan	0.656	0.656	0.196	0.196
2	G359.508-0.135	-0.492	-0.135	-56.0	-73.25	40.054	0.46	0.147	0.38	nan	nan	nan	0.844	0.844	0.139	0.139
3	G359.561-0.001	-0.439	-0.001	-90.0	-59.31	23.36	0.38	0.091	0.22	2.15	2.15	0.35	0.708	0.708	0.157	0.157
4a	G359.595-0.223	-0.405	-0.223	-27.0	-79.52	34.939	0.37	0.131	0.43	nan	nan	nan	0.536	0.536	0.249	0.249
4b	G359.595-0.223	-0.405	-0.223	-20.0	-78.19	40.247	0.36	0.145	0.26	nan	nan	nan	0.498	0.498	0.277	0.277
5	G359.608+0.018	-0.392	0.018	-78.0	-79.45	18.421	0.38	0.099	0.18	0.52	0.52	0.01	0.962	0.962	0.119	0.119
6a	G359.688-0.132	-0.312	-0.132	-29.0	-52.41	20.782	0.4	0.076	0.62	3.3	3.3	0.66	0.977	0.977	0.154	0.154
6b	G359.688-0.132	-0.312	-0.132	-21.0	-61.84	30.72	0.41	0.084	0.28	2.28	2.28	0.26	1.041	1.041	0.097	0.097
7a	G359.701+0.032	-0.299	0.032	-73.0	-96.86	26.109	0.46	0.087	-0.54	0.36	0.36	0.03	0.969	0.969	0.095	0.095
7b	G359.701+0.032	-0.299	0.032	-37.0	-91.8	30.474	0.47	0.125	-0.62	1.88	1.88	0.22	0.872	0.872	0.112	0.112
8a	G359.865+0.023	-0.135	0.023	-54.0	-113.79	50.639	0.66	0.154	-0.05	2.4	2.4	0.39	nan	nan	nan	nan
8b	G359.865+0.023	-0.135	0.023	15.0	-156.73	34.166	0.79	0.112	nan	34.87	34.87	601.01	nan	nan	nan	nan
8c	G359.865+0.023	-0.135	0.023	62.0	-157.19	32.632	0.79	0.101	-0.64	2.81	2.81	0.41	nan	nan	nan	nan
9	G359.88-0.081	-0.12	-0.081	15.0	-5.06	47.509	0.31	0.085	0.6	3.45	3.45	3.55	nan	nan	nan	nan
10	G359.979-0.071	-0.021	-0.071	48.0	38.37	69.886	0.46	0.147	0.26	0.78	0.78	0.24	nan	nan	nan	nan
11a	G0.014-0.016	0.014	-0.016	-11.0	-148.38	97.611	0.86	0.18	-0.36	2.78	2.78	0.87	nan	nan	nan	nan
11b	G0.014-0.016	0.014	-0.016	45.0	-177.87	86.135	0.92	0.166	-0.35	2.8	2.8	1.98	nan	nan	nan	nan
11c	G0.014-0.016	0.014	-0.016	14.0	-140.24	45.786	0.84	0.086	-0.92	2.62	2.62	0.05	0.869	0.869	0.068	0.068
12	G0.035+0.032	0.035	0.032	86.0	-156.53	121.741	0.86	0.274	-0.28	3.87	3.87	0.58	0.904	0.904	0.164	0.164
13	G0.068-0.076	0.068	-0.076	50.0	-65.96	33.614	0.57	0.097	0.14	1.06	1.06	0.07	nan	nan	nan	nan
14	G0.105-0.08	0.105	-0.08	53.0	-14.0	28.949	0.34	0.077	0.5	1.14	1.14	0.05	nan	nan	nan	nan
15	G0.116+0.003	0.116	0.003	52.0	-144.13	112.682	0.83	0.244	0.04	3.38	3.38	0.32	0.984	0.984	0.163	0.163
16a	G0.143-0.083	0.143	-0.083	-15.0	nan	nan	nan	nan	nan	nan	nan	nan	nan	nan	nan	nan
16b	G0.143-0.083	0.143	-0.083	57.0	-16.52	15.977	0.35	0.044	-0.06	0.89	0.89	0.17	1.041	1.041	0.103	0.103
17a	G0.255+0.02	0.255	0.02	18.0	53.12	31.617	0.2	0.124	0.65	0.28	0.28	0.04	0.707	0.707	0.177	0.177
17b	G0.255+0.02	0.255	0.02	37.0	74.09	38.177	0.2	0.108	0.72	0.31	0.31	0.03	0.564	0.564	0.134	0.134

Table 4 continued

Table 4 (continued)

leaf id	cloud name	l	b	v	flux diff	flux diff	flux ratio	flux ratio	corr coeff	absorption	absorption	star count	star count
		deg	deg	km/s	MJy/sr	MJy/sr	stdv	stdv	stdv	fraction	fraction σ	ratio	ratio stdv
17c	G0.255+0.02	0.255	0.02	70.0	56.12	22.608	0.31	0.059	0.87	1.63	0.05	0.597	0.036
18	G0.327-0.195	0.327	-0.195	16.0	-98.34	42.062	0.34	0.245	0.1	nan	nan	0.567	0.203
19	G0.342+0.06	0.342	0.06	-2.0	-57.98	48.867	0.34	0.15	0.75	0.23	0.01	0.878	0.111
20	G0.342-0.085	0.342	-0.085	90.0	-126.21	62.454	0.68	0.224	-0.33	2.21	0.55	0.991	0.13
21a	G0.379+0.05	0.379	0.05	8.0	-41.39	19.633	0.16	0.072	0.54	0.38	0.02	0.769	0.04
21b	G0.379+0.05	0.379	0.05	39.0	-25.27	20.49	0.17	0.069	0.26	1.09	0.06	0.856	0.077
22	G0.413+0.048	0.413	0.048	19.0	-49.32	14.361	0.09	0.064	0.84	0.15	0.01	0.656	0.127
23	G0.488+0.008	0.488	0.008	28.0	-39.11	22.333	0.08	0.054	0.64	0.35	0.1	0.446	0.086
24	G0.645+0.03	0.645	0.03	53.0	-97.56	2.348	-0.25	0.019	0.62	0.53	0.03	0.491	0.1
25	G0.666-0.028	0.666	-0.028	62.0	-78.28	15.046	-0.18	0.193	-0.33	2.12	0.84	0.549	0.117
26a	G0.716-0.09	0.716	-0.09	28.0	-101.03	12.295	-0.17	0.117	0.32	nan	nan	0.639	0.084
26b	G0.716-0.09	0.716	-0.09	58.0	-105.37	6.36	-0.24	0.067	0.42	nan	nan	0.627	0.074
27	G0.816-0.185	0.816	-0.185	39.0	-117.03	6.211	-0.39	0.089	0.1	nan	nan	0.856	0.096
28a	G0.888-0.044	0.888	-0.044	14.0	-114.84	4.182	-0.23	0.043	-0.94	nan	nan	1.156	0.072
28b	G0.888-0.044	0.888	-0.044	26.0	-114.84	4.182	-0.23	0.043	-0.94	nan	nan	1.156	0.072
28c	G0.888-0.044	0.888	-0.044	84.0	-113.75	4.022	-0.28	0.065	0.04	nan	nan	0.863	0.181
29a	G1.075-0.049	1.075	-0.049	74.0	-163.86	49.3	0.45	0.497	-0.23	nan	nan	0.482	0.123
29b	G1.075-0.049	1.075	-0.049	85.0	-116.07	9.506	-0.13	0.175	-0.01	nan	nan	0.629	0.28
30a	G1.601+0.012	1.601	0.012	48.0	-117.92	2.494	-0.76	0.047	0.34	nan	nan	0.781	0.23
30b	G1.601+0.012	1.601	0.012	58.0	-118.97	3.29	-0.74	0.059	0.15	nan	nan	0.872	0.261
31	G1.652-0.052	1.652	-0.052	50.0	-114.32	3.079	-0.8	0.053	0.94	nan	nan	0.531	0.15

REFERENCES

- Aizawa, M., Muto, T., & Momose, M. 2025, arXiv e-prints, arXiv:2512.16091, doi: [10.48550/arXiv.2512.16091](https://doi.org/10.48550/arXiv.2512.16091)
- Armillotta, L., Krumholz, M. R., Di Teodoro, E. M., & McClure-Griffiths, N. M. 2019, MNRAS, 490, 4401, doi: [10.1093/mnras/stz2880](https://doi.org/10.1093/mnras/stz2880)
- Astropy Collaboration, Robitaille, T. P., Tollerud, E. J., et al. 2013, A&A, 558, A33, doi: [10.1051/0004-6361/201322068](https://doi.org/10.1051/0004-6361/201322068)
- Astropy Collaboration, Price-Whelan, A. M., Sipőcz, B. M., et al. 2018, AJ, 156, 123, doi: [10.3847/1538-3881/aabc4f](https://doi.org/10.3847/1538-3881/aabc4f)
- Astropy Collaboration, Price-Whelan, A. M., Lim, P. L., et al. 2022, apj, 935, 167, doi: [10.3847/1538-4357/ac7c74](https://doi.org/10.3847/1538-4357/ac7c74)
- Athanassoula, E. 1992, MNRAS, 259, 345, doi: [10.1093/mnras/259.2.345](https://doi.org/10.1093/mnras/259.2.345)
- Balbus, S. A., & Hawley, J. F. 1998, Reviews of Modern Physics, 70, 1, doi: [10.1103/RevModPhys.70.1](https://doi.org/10.1103/RevModPhys.70.1)
- Bally, J., Aguirre, J., Battersby, C., et al. 2010, ApJ, 721, 137, doi: [10.1088/0004-637X/721/1/137](https://doi.org/10.1088/0004-637X/721/1/137)
- Battersby, C., Walker, D. L., Barnes, A., et al. 2025a, The Astrophysical Journal, 984, 156, doi: [10.3847/1538-4357/adb5f0](https://doi.org/10.3847/1538-4357/adb5f0)
- . 2025b, The Astrophysical Journal, 984, 157, doi: [10.3847/1538-4357/adb844](https://doi.org/10.3847/1538-4357/adb844)
- Benjamin, R. A., Churchwell, E., Babler, B. L., et al. 2003, PASP, 115, 953, doi: [10.1086/376696](https://doi.org/10.1086/376696)
- Binney, J., Gerhard, O. E., Stark, A. A., Bally, J., & Uchida, K. I. 1991, MNRAS, 252, 210, doi: [10.1093/mnras/252.2.210](https://doi.org/10.1093/mnras/252.2.210)
- Blaylock-Squibbs, G. A., & Parker, R. J. 2023, MNRAS, 519, 3643, doi: [10.1093/mnras/stac3683](https://doi.org/10.1093/mnras/stac3683)
- Buta, R., & Combes, F. 1996, FCPh, 17, 95
- Butterfield, N. O., Chuss, D. T., Guerra, J. A., et al. 2024, ApJ, 963, 130, doi: [10.3847/1538-4357/ad12b9](https://doi.org/10.3847/1538-4357/ad12b9)
- Callanan, D., Longmore, S. N., Kruijssen, J. M. D., et al. 2021, MNRAS, 505, 4310, doi: [10.1093/mnras/stab1527](https://doi.org/10.1093/mnras/stab1527)
- Chaves-Velasquez, L., Gómez, G. C., & Pérez-Villegas, Á. 2025, PASA, 42, e014, doi: [10.1017/pasa.2024.130](https://doi.org/10.1017/pasa.2024.130)
- Chuard, D., Terrier, R., Goldwurm, A., et al. 2018, A&A, 610, A34, doi: [10.1051/0004-6361/201731864](https://doi.org/10.1051/0004-6361/201731864)
- Churchwell, E., Babler, B. L., Meade, M. R., et al. 2009, PASP, 121, 213, doi: [10.1086/597811](https://doi.org/10.1086/597811)
- Clavel, M., Terrier, R., Goldwurm, A., et al. 2013, A&A, 558, A32, doi: [10.1051/0004-6361/201321667](https://doi.org/10.1051/0004-6361/201321667)
- Contopoulos, G., & Grosbol, P. 1989, A&A Rv, 1, 261, doi: [10.1007/BF00873080](https://doi.org/10.1007/BF00873080)
- Davies, R. I., Müller Sánchez, F., Genzel, R., et al. 2007, ApJ, 671, 1388, doi: [10.1086/523032](https://doi.org/10.1086/523032)
- Edenhofer, G., Zucker, C., Frank, P., et al. 2024, A&A, 685, A82, doi: [10.1051/0004-6361/202347628](https://doi.org/10.1051/0004-6361/202347628)
- Ellsworth-Bowers, T. P., Glenn, J., Rosolowsky, E., et al. 2013, ApJ, 770, 39, doi: [10.1088/0004-637X/770/1/39](https://doi.org/10.1088/0004-637X/770/1/39)
- Ellsworth-Bowers, T. P., Glenn, J., Riley, A., et al. 2015, ApJ, 805, 157, doi: [10.1088/0004-637X/805/2/157](https://doi.org/10.1088/0004-637X/805/2/157)
- Gallego-Cano, E., Schödel, R., Noguera-Lara, F., et al. 2020, A&A, 634, A71, doi: [10.1051/0004-6361/201935303](https://doi.org/10.1051/0004-6361/201935303)
- Genzel, R., Eisenhauer, F., & Gillessen, S. 2010, Reviews of Modern Physics, 82, 3121, doi: [10.1103/RevModPhys.82.3121](https://doi.org/10.1103/RevModPhys.82.3121)
- Genzel, R., Stacey, G. J., Harris, A. I., et al. 1990, ApJ, 356, 160, doi: [10.1086/168827](https://doi.org/10.1086/168827)
- Ginsburg, A., Walsh, A., Henkel, C., et al. 2015, A&A, 584, L7, doi: [10.1051/0004-6361/201527452](https://doi.org/10.1051/0004-6361/201527452)
- Ginsburg, A., Henkel, C., Ao, Y., et al. 2016, A&A, 586, A50, doi: [10.1051/0004-6361/201526100](https://doi.org/10.1051/0004-6361/201526100)
- Gleis, D. R., Stuber, S. K., Schinnerer, E., et al. 2026, arXiv e-prints, arXiv:2601.11127, doi: [10.48550/arXiv.2601.11127](https://doi.org/10.48550/arXiv.2601.11127)
- Gramze, S. R., Ginsburg, A., Meier, D. S., et al. 2023, ApJ, 959, 93, doi: [10.3847/1538-4357/ad01be](https://doi.org/10.3847/1538-4357/ad01be)
- GRAVITY Collaboration, Abuter, R., Amorim, A., et al. 2021, A&A, 647, A59, doi: [10.1051/0004-6361/202040208](https://doi.org/10.1051/0004-6361/202040208)
- Hatano, H., Nishiyama, S., Kurita, M., et al. 2013, AJ, 145, 105, doi: [10.1088/0004-6256/145/4/105](https://doi.org/10.1088/0004-6256/145/4/105)
- Henshaw, J. D., Barnes, A. T., Battersby, C., et al. 2023, in Astronomical Society of the Pacific Conference Series, Vol. 534, Protostars and Planets VII, ed. S. Inutsuka, Y. Aikawa, T. Muto, K. Tomida, & M. Tamura, 83, doi: [10.48550/arXiv.2203.11223](https://doi.org/10.48550/arXiv.2203.11223)
- Henshaw, J. D., Longmore, S. N., & Kruijssen, J. M. D. 2016a, MNRAS, 463, L122, doi: [10.1093/mnrasl/slw168](https://doi.org/10.1093/mnrasl/slw168)
- Henshaw, J. D., Longmore, S. N., Kruijssen, J. M. D., et al. 2016b, MNRAS, 457, 2675, doi: [10.1093/mnras/stw121](https://doi.org/10.1093/mnras/stw121)
- Henshaw, J. D., Kruijssen, J. M. D., Longmore, S. N., et al. 2020, Nature Astronomy, 4, 1064, doi: [10.1038/s41550-020-1126-z](https://doi.org/10.1038/s41550-020-1126-z)
- Herrnstein, R. M., & Ho, P. T. P. 2005, ApJ, 620, 287, doi: [10.1086/426047](https://doi.org/10.1086/426047)
- Jones, P. A., Burton, M. G., Cunningham, M. R., et al. 2012, MNRAS, 419, 2961, doi: [10.1111/j.1365-2966.2011.19941.x](https://doi.org/10.1111/j.1365-2966.2011.19941.x)
- Kantorovich, L. 1942, Akad. Nauk SSSR, 37
- Karlsson, R., Sjouwerman, L. O., Sandqvist, A., & Whiteoak, J. B. 2003, A&A, 403, 1011, doi: [10.1051/0004-6361:20030309](https://doi.org/10.1051/0004-6361:20030309)
- Kim, W.-T., & Elmegreen, B. G. 2017, ApJL, 841, L4, doi: [10.3847/2041-8213/aa70a1](https://doi.org/10.3847/2041-8213/aa70a1)
- Krieger, N., Ott, J., Beuther, H., et al. 2017, ApJ, 850, 77, doi: [10.3847/1538-4357/aa951c](https://doi.org/10.3847/1538-4357/aa951c)

- Kruijssen, J. M. D., Dale, J. E., & Longmore, S. N. 2015, *MNRAS*, 447, 1059, doi: [10.1093/mnras/stu2526](https://doi.org/10.1093/mnras/stu2526)
- Kruijssen, J. M. D., & Longmore, S. N. 2013, *MNRAS*, 435, 2598, doi: [10.1093/mnras/stt1634](https://doi.org/10.1093/mnras/stt1634)
- Kumar, K. 2023, arXiv e-prints, arXiv:2305.00351, doi: [10.48550/arXiv.2305.00351](https://doi.org/10.48550/arXiv.2305.00351)
- Launhardt, R., Zylka, R., & Mezger, P. G. 2002, *A&A*, 384, 112, doi: [10.1051/0004-6361:20020017](https://doi.org/10.1051/0004-6361:20020017)
- Lee, S., Pak, S., Choi, M., et al. 2008, *The Astrophysical Journal*, 674, 247, doi: [10.1086/524128](https://doi.org/10.1086/524128)
- Levy, R. 2022, in *American Astronomical Society Meeting Abstracts*, Vol. 240, American Astronomical Society Meeting #240, 130.07
- Lipman, D., Battersby, C., Walker, D. L., et al. 2025, *The Astrophysical Journal*, 984, 159, doi: [10.3847/1538-4357/adb5ee](https://doi.org/10.3847/1538-4357/adb5ee)
- Longmore, S. N., Bally, J., Testi, L., et al. 2013, *MNRAS*, 429, 987, doi: [10.1093/mnras/sts376](https://doi.org/10.1093/mnras/sts376)
- Mahalanobis, P. 1936, *Sankhya A*, 80, 1 .
<https://api.semanticscholar.org/CorpusID:239595337>
- Marin, F., Churazov, E., Khabibullin, I., et al. 2023, *Nature*, 619, 41, doi: [10.1038/s41586-023-06064-x](https://doi.org/10.1038/s41586-023-06064-x)
- Martínez-Arranz, Á., Schödel, R., Nogueras-Lara, F., & Shahzamanian, B. 2022, *A&A*, 660, L3, doi: [10.1051/0004-6361/202243263](https://doi.org/10.1051/0004-6361/202243263)
- Mills, E. A. C., Ginsburg, A., Immer, K., et al. 2018, *ApJ*, 868, 7, doi: [10.3847/1538-4357/aae581](https://doi.org/10.3847/1538-4357/aae581)
- Mokeddem, R., Lopes, M., Avila, F., Bernui, A., & Hipólito-Ricaldi, W. S. 2026, *Physics of the Dark Universe*, 51, 102185, doi: [10.1016/j.dark.2025.102185](https://doi.org/10.1016/j.dark.2025.102185)
- Molinari, S., Swinyard, B., Bally, J., et al. 2010, *A&A*, 518, L100, doi: [10.1051/0004-6361/201014659](https://doi.org/10.1051/0004-6361/201014659)
- Molinari, S., Bally, J., Noriega-Crespo, A., et al. 2011, *ApJL*, 735, L33, doi: [10.1088/2041-8205/735/2/L33](https://doi.org/10.1088/2041-8205/735/2/L33)
- Molinari, S., Schisano, E., Elia, D., et al. 2016, *A&A*, 591, A149, doi: [10.1051/0004-6361/201526380](https://doi.org/10.1051/0004-6361/201526380)
- Monge, G. 1781, *Mem. Math. Phys. Acad. Royale Sci.*, 666
- Nagayama, T., Nagashima, C., Nakajima, Y., et al. 2003, in *Society of Photo-Optical Instrumentation Engineers (SPIE) Conference Series*, Vol. 4841, *Instrument Design and Performance for Optical/Infrared Ground-based Telescopes*, ed. M. Iye & A. F. M. Moorwood, 459–464, doi: [10.1117/12.460770](https://doi.org/10.1117/12.460770)
- Newville, M., Otten, R., Nelson, A., et al. 2025, *LMFIT: Non-Linear Least-Squares Minimization and Curve-Fitting for Python*, 1.3.3, Zenodo, doi: [10.5281/zenodo.15014437](https://doi.org/10.5281/zenodo.15014437)
- Nishiyama, S., & Schödel, R. 2013, *A&A*, 549, A57, doi: [10.1051/0004-6361/201219773](https://doi.org/10.1051/0004-6361/201219773)
- Nishiyama, S., Yasui, K., Nagata, T., et al. 2013, *ApJL*, 769, L28, doi: [10.1088/2041-8205/769/2/L28](https://doi.org/10.1088/2041-8205/769/2/L28)
- Nogueras-Lara, F. 2022, *A&A*, 668, L8, doi: [10.1051/0004-6361/202244934](https://doi.org/10.1051/0004-6361/202244934)
- Nogueras-Lara, F., Schödel, R., Neumayer, N., & Schultheis, M. 2021, *A&A*, 647, L6, doi: [10.1051/0004-6361/202140554](https://doi.org/10.1051/0004-6361/202140554)
- Nogueras-Lara, F., Barnes, A. T., Henshaw, J. D., et al. 2026, *A&A*, 706, A18, doi: [10.1051/0004-6361/202556047](https://doi.org/10.1051/0004-6361/202556047)
- Pearson, K., & Galton, F. 1895, *Proceedings of the Royal Society of London*, 58, 240, doi: [10.1098/rspl.1895.0041](https://doi.org/10.1098/rspl.1895.0041)
- Pedlar, A., Anantharamaiah, K. R., Ekers, R. D., et al. 1989, *ApJ*, 342, 769, doi: [10.1086/167635](https://doi.org/10.1086/167635)
- Pillai, T., Kauffmann, J., Tan, J. C., et al. 2015, *ApJ*, 799, 74, doi: [10.1088/0004-637X/799/1/74](https://doi.org/10.1088/0004-637X/799/1/74)
- Ponti, G., Terrier, R., Goldwurm, A., Belanger, G., & Trap, G. 2010, in *AAS/High Energy Astrophysics Division*, Vol. 11, *AAS/High Energy Astrophysics Division #11*, 11.12
- Reid, M. J., Menten, K. M., Zheng, X. W., Brunthaler, A., & Xu, Y. 2009, *ApJ*, 705, 1548, doi: [10.1088/0004-637X/705/2/1548](https://doi.org/10.1088/0004-637X/705/2/1548)
- Ridley, M. G. L., Sormani, M. C., Treß, R. G., Magorrian, J., & Klessen, R. S. 2017, *MNRAS*, 469, 2251, doi: [10.1093/mnras/stx944](https://doi.org/10.1093/mnras/stx944)
- Robitaille, T., Rice, T., Beaumont, C., et al. 2019, *astrodendro: Astronomical data dendrogram creator*, *Astrophysics Source Code Library*, record ascl:1907.016. <http://ascl.net/1907.016>
- Ryu, S. G., Nobukawa, M., Nakashima, S., et al. 2013, *PASJ*, 65, 33, doi: [10.1093/pasj/65.2.33](https://doi.org/10.1093/pasj/65.2.33)
- Salas, J. M., Naoz, S., & Morris, M. R. 2020, arXiv e-prints, arXiv:2010.04170, doi: [10.48550/arXiv.2010.04170](https://doi.org/10.48550/arXiv.2010.04170)
- Sawada, T., Hasegawa, T., Handa, T., & Cohen, R. J. 2004, *MNRAS*, 349, 1167, doi: [10.1111/j.1365-2966.2004.07603.x](https://doi.org/10.1111/j.1365-2966.2004.07603.x)
- Schödel, R., Feldmeier, A., Kunneriath, D., et al. 2014, *A&A*, 566, A47, doi: [10.1051/0004-6361/201423481](https://doi.org/10.1051/0004-6361/201423481)
- Shlosman, I., Frank, J., & Begelman, M. C. 1989, *Nature*, 338, 45, doi: [10.1038/338045a0](https://doi.org/10.1038/338045a0)
- Sofue, Y. 1995, *PASJ*, 47, 527. <https://arxiv.org/abs/astro-ph/9508110>
- . 2022, *MNRAS*, 516, 907, doi: [10.1093/mnras/stac2243](https://doi.org/10.1093/mnras/stac2243)
- Sofue, Y., Oka, T., Longmore, S. N., et al. 2025, arXiv e-prints, arXiv:2504.03331, doi: [10.48550/arXiv.2504.03331](https://doi.org/10.48550/arXiv.2504.03331)
- Sormani, M. C., Binney, J., & Magorrian, J. 2015, *MNRAS*, 449, 2421, doi: [10.1093/mnras/stv441](https://doi.org/10.1093/mnras/stv441)
- Sormani, M. C., Magorrian, J., Nogueras-Lara, F., et al. 2020a, *MNRAS*, 499, 7, doi: [10.1093/mnras/staa2785](https://doi.org/10.1093/mnras/staa2785)

- Sormani, M. C., Tress, R. G., Glover, S. C. O., et al. 2020b, MNRAS, 497, 5024, doi: [10.1093/mnras/staa1999](https://doi.org/10.1093/mnras/staa1999)
- Sormani, M. C., Sanders, J. L., Fritz, T. K., et al. 2022, MNRAS, 512, 1857, doi: [10.1093/mnras/stac639](https://doi.org/10.1093/mnras/stac639)
- Stel, G., Ponti, G., Haardt, F., & Sormani, M. 2025, A&A, 695, A52, doi: [10.1051/0004-6361/202451359](https://doi.org/10.1051/0004-6361/202451359)
- Stuber, S. K., Schinnerer, E., Williams, T. G., et al. 2023, A&A, 676, A113, doi: [10.1051/0004-6361/202346318](https://doi.org/10.1051/0004-6361/202346318)
- Sun, J., Leroy, A. K., Schinnerer, E., et al. 2020, ApJL, 901, L8, doi: [10.3847/2041-8213/abb3be](https://doi.org/10.3847/2041-8213/abb3be)
- Sun, J., He, H., Batschkun, K., et al. 2024, ApJ, 967, 133, doi: [10.3847/1538-4357/ad3de6](https://doi.org/10.3847/1538-4357/ad3de6)
- Sunyaev, R., & Churazov, E. 1998, MNRAS, 297, 1279, doi: [10.1046/j.1365-8711.1998.01684.x](https://doi.org/10.1046/j.1365-8711.1998.01684.x)
- Tress, R. G., Sormani, M. C., Glover, S. C. O., et al. 2020, MNRAS, 499, 4455, doi: [10.1093/mnras/staa3120](https://doi.org/10.1093/mnras/staa3120)
- Tress, R. G., Sormani, M. C., Girichidis, P., et al. 2024, A&A, 691, A303, doi: [10.1051/0004-6361/202450035](https://doi.org/10.1051/0004-6361/202450035)
- Tsuboi, M., Kitamura, Y., Uehara, K., et al. 2018, PASJ, 70, 85, doi: [10.1093/pasj/psy080](https://doi.org/10.1093/pasj/psy080)
- Villani, C. 2021, Topics in optimal transportation, Vol. 58 (American Mathematical Soc.)
- Walker, D. L., Battersby, C., Lipman, D., et al. 2025, The Astrophysical Journal, 984, 158, doi: [10.3847/1538-4357/adb5ef](https://doi.org/10.3847/1538-4357/adb5ef)
- Yan, Q.-Z., Walsh, A. J., Dawson, J. R., et al. 2017, MNRAS, 471, 2523, doi: [10.1093/mnras/stx1724](https://doi.org/10.1093/mnras/stx1724)
- Yasui, K., Nishiyama, S., Yoshikawa, T., et al. 2015, PASJ, 67, 123, doi: [10.1093/pasj/psv100](https://doi.org/10.1093/pasj/psv100)
- Yusef-Zadeh, F., & Morris, M. 1987, ApJ, 320, 545, doi: [10.1086/165572](https://doi.org/10.1086/165572)
- Zhang, M., Kainulainen, J., Zhao, H., et al. 2025, MNRAS, 543, 3830, doi: [10.1093/mnras/staf1704](https://doi.org/10.1093/mnras/staf1704)
- Zoccali, M., Valenti, E., Surot, F., et al. 2021, MNRAS, 502, 1246, doi: [10.1093/mnras/stab089](https://doi.org/10.1093/mnras/stab089)